

1 Global 1km Land Surface Parameters for Kilometer-Scale Earth System Modeling

2 Lingcheng Li, Gautam Bisht, Dalei Hao, L. Ruby Leung

3 Atmospheric, Climate, and Earth Sciences Division, Pacific Northwest National Laboratory,
4 Richland, WA, USA

5

6 Correspondence: Lingcheng Li (lingcheng.li@pnnl.gov) and Gautam Bisht
7 (gautam.bisht@pnnl.gov)

8

9 **Abstract**

10 Earth system models (ESMs) are progressively advancing towards the kilometer scale (k-scale).
11 However, the surface parameters for Land Surface Models (LSMs) within ESMs running at the k-
12 scale are typically derived from coarse resolution and outdated datasets. This study aims to develop
13 a new set of global land surface parameters with a resolution of 1 km for multiple years from 2001
14 to 2020, utilizing the latest and most accurate available datasets. Specifically, the datasets consist
15 of parameters related to land use and land cover, vegetation, soil, and topography. Differences
16 between the newly developed 1k land surface parameters and conventional parameters emphasize
17 their potential for higher accuracy due to the incorporation of the most advanced and latest data
18 sources. To demonstrate the capability of these new parameters, we conducted 1 km resolution
19 simulations using the E3SM Land Model version 2 (ELM2) over the contiguous United States.
20 Our results demonstrate that land surface parameters contribute to significant spatial heterogeneity
21 in ELM2 simulations of soil moisture, latent heat, emitted longwave radiation, and absorbed
22 shortwave radiation. On average, about 31% to 54% of spatial information is lost by upscaling the
23 1 km ELM2 simulations to a 12 km resolution. Using eXplainable Machine Learning (XML)
24 methods, the influential factors driving the spatial variability and spatial information loss of ELM2
25 simulations were identified, highlighting the substantial impact of the spatial variability and
26 information loss of various land surface parameters, as well as the mean climate conditions. [The
27 comparison against four benchmark datasets indicates that ELM generally performs well in
28 simulating soil moisture and surface energy fluxes.](#) The new land surface parameters are tailored
29 to meet the emerging needs of k-scale LSMs and ESMs modeling with significant implications for
30 advancing our understanding of water, carbon, and energy cycles under global change. The 1 km
31 land surface parameters are publicly available at <https://zenodo.org/records/10523833> (Li et al.,
32 [2024](#)).

Deleted: <https://doi.org/10.25584/PNNLDH/1986308> (Li et al., 2023)...

35 **1. Introduction**

36 Aided by advancements in computing power, it has become increasingly feasible to run land
37 surface models (LSMs) and Earth system models (ESMs) at the kilometer scale (k-scale) to
38 improve our understanding of Earth system processes. The emergence of k-scale modeling has the
39 potential to improve the accuracy of climate simulations significantly and allow for explicit
40 modeling of physical processes that were previously poorly represented in climate models (Nat.
41 Clim. Chang. 2022), such as modeling of mesoscale convective systems in the atmosphere (Slingo
42 et al., 2022) and mesoscale eddies in ocean (Hewitt et al., 2022). Simultaneously, land modeling
43 has also witnessed a surge of interest in hyper-resolution modeling, initially proposed by Wood et
44 al. (2011), which aims to model land surface processes at a horizontal resolution of 1 km globally
45 and 100 m or finer for continental or regional domains. The motivation behind hyper-resolution
46 modeling is to address the requirements of operational forecasting like extreme events, and to
47 enhance our understanding of hydrological and biogeochemical cycling, and land–atmosphere
48 interactions. High-resolution LSMs have been increasingly applied in various fields, as
49 demonstrated by recent examples, such as 30-meter soil moisture simulations over the contiguous
50 United States (CONUS) (Vergopolan et al., 2020, 2021, 2022), 500-meter hyper-resolution
51 modeling of surface and root zone soil moisture over Oklahoma (Rouf et al., 2021), 1-km
52 simulations over Southwestern US (Singh et al., 2015), 3-km simulations over eastern Tibetan
53 Plateau to understand hydrological changes over mountainous regions (Yuan et al., 2018; Ji and
54 Yuan, 2018), 6-km simulations over China to reduce simulations errors of hydrological variables
55 (Ji et al., 2023). High-resolution modeling can better capture the land surface heterogeneity and
56 could improve simulations of terrestrial water and energy cycles (Giorgi and Avissar, 1997;
57 Chaney et al., 2018; Xu et al., 2023), biogeochemical cycles (Chaney et al., 2018), as well as land–

58 atmosphere coupling (Liu et al., 2017; Zhou et al., 2019; Bou-Zeid et al., 2020). For example,
59 Singh et al. (2015) demonstrated that increasingly capturing topography and soil texture
60 heterogeneity at finer resolutions (e.g., 1 km) improves land surface modeling of water and energy
61 variables. Li et al. (2022) have shown that the spatial heterogeneities of land surface parameters
62 (including land use and land cover (LULC) and topography) are essential for modeling the spatial
63 variability of land surface energy and water partitioning. Hao et al. (2022) found that 1 km
64 simulations with sub-grid topographic configurations can better capture the topographic effects on
65 surface fluxes.

66
67 The parameters for LSMs within ESMs being run at the k-scale are typically derived from coarse
68 resolution datasets or outdated datasets. Consequently, k-scale modeling may not accurately
69 represent fine-scale land surface heterogeneity unless high-resolution land surface parameters at
70 the kilometer or finer scales are utilized. Publicly available land surface parameters are primarily
71 provided at coarse resolutions and based on outdated datasets (see details in Table 1). For example,
72 the Community Land Model version 5 (CLM5; Lawrence et al., 2019) typically relies on land
73 surface parameters with spatial resolutions ranging from 1km to 0.5° based on source datasets that
74 were processed more than 10 years ago (see Table 1 for details). Although LULC-related
75 parameters are available at a relatively high resolution of 0.05°, they are temporally static and were
76 derived from a combination of data from different years spanning 1993 to 2012 (Table 1). Leaf
77 area index (LAI) was derived from the now outdated products of Moderate Resolution Imaging
78 Spectroradiometer (MODIS) collection 4 (Myneni et al., 2002). The canopy height for tree Plant
79 Functional Types (PFTs) is based on forest canopy height data derived from the Geoscience Laser
80 Altimeter System (GLAS) aboard ICESat, collected in 2005 (Simard et al., 2011). Canopy height

81 for short vegetation is represented by PFT-specific values that remain invariant in space (Bonan et
82 al., 2002). Soil sand and clay content were obtained from the International Geosphere-Biosphere
83 Programme (IGBP) soil dataset (Global Soil Data Task 2000) consisting of 4931 soil mapping
84 units (IGBP, 2000). These CLM5 land surface parameters have been widely utilized in the LSMs
85 and ESMs communities, despite being developed over a decade ago. Subsequently, Ke et al. (2012;
86 hereafter referred to as K2012) developed an updated set of LULC and vegetation-related land
87 surface parameters for CLM4 at a resolution of 0.05°. These parameters were developed based on
88 MODIS collection 5 products or datasets derived from MODIS collection 5 products, including
89 PFTs and non-vegetation land cover, LAI, and Stem Area Index (SAI). K2012 has also been widely
90 used by LSMs, including CLM (e.g., Leng et al., 2013; Ke et al., 2013; Singh et al., 2015; Xia et
91 al., 2017) and the Energy Exascale Earth System Model (E3SM) Land Model (ELM) (e.g.,
92 Caldwell et al., 2019; Leung et al., 2020; Li et al., 2022). However, the CLM5 and K2012 datasets,
93 with their relatively coarse resolution and reliance on outdated data from over a decade ago, may
94 not fully meet the requirements for k-scale modeling. Additionally, these datasets include LULC,
95 LAI, and SAI that are year invariant. Consequently, they are inappropriate for studies involving
96 LULC changes, such as urbanization. In addition, some recently developed land surface processes
97 and their associated parameters are not included in previous datasets. For instance, Hao et al. (2021)
98 introduced a sub-grid topographic parameterization of solar radiation with five associated
99 topographic factors in ELM, which have been found to significantly affect the surface energy
100 budget. the surface energy budget.

101
102 High-resolution and up-to-date datasets at kilometer or finer resolutions are now widely available
103 and can be utilized to derive more accurate land surface parameters for k-scale LSM simulations.

104 For example, the MODIS Land Cover Type Collection 6 (MCD12Q1 C6) data product provides
105 global land cover types yearly from 2001 to the present (Friedl et al., 2019; Sulla-Menashe et al.,
106 2019) at 500-meter resolution. Compared to the MODIS Collection 4 (used in CLM5 land surface
107 parameters) and Collection 5 products (used in K2012 land surface parameters), the C6 data
108 represents a significant advancement in algorithm improvements and the quality of land cover
109 information. Despite the availability of high-resolution MODIS LAI products, such as the 500 m
110 MCD15A2H (Myneni et al., 2021), they suffer from noise and gaps with spatially and temporally
111 inconsistent values due to clouds, seasonal snow cover, instrument issues, and uncertainties in
112 retrieval algorithms (Yuan et al., 2011). To address these limitations, Yuan et al. (2011)
113 reprocessed MODIS LAI products and generated a more accurate and spatiotemporally continuous
114 and consistent LAI dataset that is available continuously to the present period. Additional high-
115 resolution and up-to-date datasets are available for preparing land surface parameters, such as soil
116 texture and soil organic matter at 250-meter resolution (Poggio et al., 2021) and vegetation height
117 at 10-m resolution (Lang et al., 2023).

118

119 This study aims to develop a new set of global land surface parameters with a resolution of 1 km
120 for multiple years, utilizing the latest and most accurate available datasets. These parameters will
121 be tailored to meet the needs of k-scale Earth system modeling. The newly developed land surface
122 parameters include four categories: (1) LULC-related parameters, such as the spatial distributions
123 of PFTs, lakes, wetlands, urban areas, and glaciers; (2) vegetation-related parameters, including
124 PFTs' LAI and SAI for multiple years ranging from 2001 to 2021, and the canopy top and bottom
125 height; (3) soil-related parameters, such as soil textures and soil organic matter; and (4)
126 topography-related parameters, such as elevation, slope, aspect, and sub-grid topographic factors.

127 We conducted a comparison of the new 1k parameters against the K2012 and ELM2/CLM5 default
128 parameters. Utilizing ELM version 2 (ELM2) as a testbed, we demonstrated the modeling
129 capability enabled by the new high-resolution parameters through a 5-year simulation at 1 km
130 resolution over the CONUS. We performed a spatial scaling analysis on four ELM2 simulated
131 variables, which included soil moisture, latent heat, emitted longwave radiation, and absorbed
132 shortwave radiation, to underscore the significance of high-resolution land surface parameters on
133 ELM2 simulations. We employed eXplainable Machine Learning (XML) methods to evaluate the
134 most important factors of land surface parameters and climate conditions (e.g., mean temperature
135 and precipitation) in driving the spatial variability and spatial information loss of ELM2
136 simulations.

137 **2. Development of 1km land surface parameters**

138 In this study, all the land surface parameters were developed globally at a resolution of
139 approximately 1 km (i.e., $1/120^\circ$, hereafter referred to as 1 km; Table 1). The LULC-related
140 parameters, soil properties, canopy height, and elevation were processed via Google Earth Engine
141 (GEE; Gorelick et al., 2017). The LAI was processed using an area-weighted average from its
142 original 450 m resolution obtained from Beijing Normal University (Yuan et al., 2011). All data
143 sources utilized in this study have been rigorously validated in their respective original
144 publications. The detailed methods for deriving these parameters are described below.

145

Table 1 Comparison between new and previous land surface parameters

Category	Land surface parameters	This study	ELM2 / CLM5 *	K2012
LULC	PFTs, Lake, Glacier, Urban	<ul style="list-style-type: none"> Resolution: 1 km, yearly, 2001-2020 Data source: 500 m, yearly, MODIS collection 6 (Friedl et al., 2019) 	<ul style="list-style-type: none"> Resolution: 0.05°, temporally static, processed based on data from mixed years PFTs data source: mixed years from 1993 to 2001; 500 m, MODIS Vegetation Continuous Fields (Hansen et al., 2003); 1 km, tree cover (Defries et al., 2000); 10 km (5 arc minutes), cropland (Ramankutty and Foley, 1999); 1 km, MODIS land cover collection 4 (Friedl et al., 2002) Lake data source: 3 km (90 arc seconds) lake data (Kourzeneva 2009, 2010) Glacier data source: glacier and ice sheet vector data (Arendt et al. 2012; Rastner et al. 2012) Urban data source: 1 km urban data (Jackson et al., 2010) 	<ul style="list-style-type: none"> Resolution: 0.05°, year 2005 Data source: 500 m, yearly, MODIS collection 5 (Friedl et al., 2010)
Vegetation	LAI, SAI	<ul style="list-style-type: none"> Resolution: 1 km, monthly, 2001-2020 Data source: 450 m, 8-day, reprocessed MODIS collection 6 LAI (Yuan et al., 2011; Friedl et al., 2019) 	<ul style="list-style-type: none"> Resolution: 0.5°, 12 months Data source: 1 km, 8-day, MODIS collection 4 LAI (Myneni et al., 2002) 	<ul style="list-style-type: none"> Resolution: 0.05°, year 2005 Data source: 450 m, 8-day, reprocessed MODIS collection 5 LAI (Yuan et al., 2011; Friedl et al., 2010)
	Canopy top height, Canopy bottom height	<ul style="list-style-type: none"> Resolution: 1 km, temporally static Data source: 10 m, vegetation canopy height (Lang et al., 2023) 	<ul style="list-style-type: none"> Resolution: 0.5° or PFT specified value, temporally static Tree PFT data source: 1 km, forest canopy height derived using 2005 GLAS aboard ICESat data (Simard et al., 2011); Short vegetation data source: PFT specific values (Bonan et al., 2002) 	--
Soil	Percent sand, Percent clay	<ul style="list-style-type: none"> Resolution: 1 km, temporally static 	<ul style="list-style-type: none"> Resolution: 10 km (0.083°), temporally static 	--
	Soil organic matter	<ul style="list-style-type: none"> Data source: 250 m, Soilgrid v2 (Poggio et al., 2021) 	<ul style="list-style-type: none"> Data source: IGBP soil data of 4931 mapping units (IGBP, 2000) 	--
Topography	Elevation, Slope, Standard deviation of elevation	<ul style="list-style-type: none"> Resolution: 1 km, temporally static Data source: 90 m, MERIT Hydro elevation (Yamazaki et al., 2019) 	<ul style="list-style-type: none"> Resolution: merge of 1 km and 10 arc minutes, temporally static Data source: global most regions are based on USGS HYDRO1k (Verdin and Greenlee 1996); but 10 arc minute data is used over Greenland and Antarctica. 	--
	Aspect, Sky view factor, Terrain configuration factor	<ul style="list-style-type: none"> Resolution: 1 km, temporally static Data source: 90 m, MERIT Hydro elevation (Yamazaki et al., 2019) 	--	--

147 * ELM2 and CLM5 share the same default land surface parameters, detailed descriptions available at:
148 https://escomp.github.io/ctsm-docs/versions/release-clm5.0/html/tech_note/index.html.

149
150

151 **2.1 LULC-related parameters**

152 In this study, the MODIS MCD12Q1 version 6 (Friedl et al., 2022) was employed to ascertain the
153 Plant Functional Types (PFT) as well as other non-vegetative land categories at a spatial resolution
154 of 1 km spanning the years 2001 to 2020. The integrity of the MODIS land cover product has been
155 established through a 10-fold cross-validation accuracy assessment using the Terrestrial
156 Ecosystem Parameterization database (Sulla-Menashe et al., 2019). This land cover product offers
157 richer and more flexible land cover data with higher accuracy and substantially less year-to-year
158 stochastic variation in classification results (Sulla-Menashe et al., 2019). Being the sole operational
159 global land cover product available with annual intervals, it addresses a significant gap in the realm
160 of global change research.

161
162 The original MODIS land cover data was first resampled to 1 km from its original 500 m resolution
163 using a majority resampling method in GEE. At such a high 1km resolution, we did not consider
164 the proportion of different land cover types within each grid. Instead, we assigned 100% of a grid
165 cell to the major land cover type. Specifically, the MCD12Q1 LC_Type 5 PFT classification layer
166 was used to determine the distributions of the seven PFTs, as well as lake, urban, and glacier,
167 following the method outlined in Ke et al. (2012) and summarized below:

- 168 • The seven PFTs include needleleaf evergreen trees, needleleaf deciduous trees, broadleaf
169 evergreen trees, broadleaf deciduous trees, shrub, grass, and crop. These PFTs were further
170 reclassified into 15 categories (Table S1) that are typically used in LSMs based on the rules
171 presented in Bonan et al. (2002a) with the assistance of 1 km precipitation and surface air
172 temperature from WorldClim V1 (Hijmans et al., 2005).

173 • Grass was reclassified as C3 and C4 grass using the approach presented by Still et al. (2003),
174 with the assistance of monthly LAI (processed in section 2.2.1) and meteorological
175 variables from WorldClim V1.

176 • The "non-vegetated land" was classified as barren soil class.

177 • The "permanent snow and ice" was assigned as the glacier land unit.

178 • Global lakes were identified based on the classification of "water bodies" over the global
179 land, constrained using the global land mask obtained from Natural Earth
180 (<https://www.naturalearthdata.com/>).

181 • The urban land unit was determined based on the MODIS "urban and built-up"
182 classification. These urban grids were further classified into three urban classes, namely,
183 tall building district (TBD), high density (HD), and medium density (MD), based on
184 Jackson et al. (2010; hereinafter referred to as J2010). J2010 generated global urban extent
185 maps for the TBD, HD, and MD classes at a spatial resolution of 1 km, based on rules of
186 building height and vegetation coverage fraction
187 (https://gdex.ucar.edu/dataset/188a_oleson/file.html). However, the J2010 dataset is
188 temporally static and cannot reflect changes in urban boundaries over time. Therefore, we
189 reclassified the yearly MODIS urban land class as TBD, HD, and MD based on the J2010
190 dataset using the nearest neighbor sampling method for each year.

191 After determining the distribution of 15 PFTs, bare soil, lake, glacier, and urban land, any
192 remaining 1 km grids were assigned as ocean (Table S1). It should be noted that the wetland land
193 unit was not explicitly classified in this study. This is because, instead of treating wetlands as an
194 individual land unit, many LSMs (e.g., ELM2 and CLM5) integrate wetland functioning processes

195 prognostically within other land units where a surface water storage component is implemented to
196 represent wetland functioning.

197

198 **2.2 Vegetation-related parameters**

199 **2.2.1 Monthly LAI and SAI**

200 The monthly LAI parameters were obtained from Beijing Normal University (BNU_LAI; Yuan et
201 al., 2011). BNU_LAI, an enhanced version of the MODIS LAI product, has been subjected to
202 thorough quality control, incorporating multiple algorithms for improved accuracy (Yuan et al.,
203 2011). Its validation involved an extensive array of LAI reference maps and employed the bottom-
204 up approach advocated by the CEOS Land Product Validation sub-group (Morisette et al., 2006).
205 Compared to the original MODIS LAI, the BNU_LAI dataset exhibits superior performance, along
206 with enhanced spatiotemporal continuity and consistency. The 8-day BNU_LAI product at a
207 resolution of 15 seconds (~450 m) over 2001–2020 was downloaded from
208 <http://globalchange.bnu.edu.cn/research/laiv061>. Subsequently, the data were resampled to a
209 resolution of 1 km using an area-weighted average method and averaged temporally for each
210 month. The processed monthly LAI at 1 km resolution was subsequently assigned to each of the
211 15 PFTs described above at each grid. The monthly SAI was then calculated based on the
212 processed monthly LAI using the methods and PFT parameters described in Zeng et al. (2002).

213

214 **2.2.2 Vegetation canopy height**

215 We leveraged a global vegetation canopy height dataset sourced from Lang et al. (2023). This
216 dataset, derived using a probabilistic deep learning model, fuses Sentinel-2 images with the Global
217 Ecosystem Dynamics Investigation (GEDI) to retrieve canopy height. It stands out as the inaugural

218 global canopy height dataset offering consistent, wall-to-wall coverage at a 10 m spatial resolution
219 across all vegetation types. Assessments using hold-out GEDI reference data and comparisons
220 with independent airborne LiDAR data demonstrate that the approach outlined by Lang et al. (2023)
221 produces a meticulously quality-controlled, state-of-the-art global map product, accompanied by
222 quantitative uncertainty estimates. The canopy height served as the canopy top height parameter.
223 Canopy bottom height was calculated by multiplying PFT-based ratios derived from the ratio of
224 ELM2's (same as CLM5) canopy top and bottom heights for different PFTs (Table S2).

225

226 **2.3 Soil-related parameters**

227 We obtained the Soilgrid v2 data with an original resolution of 250 m (Poggio et al., 2021) to
228 prepare soil properties. Soilgrid is generated using machine learning based on multiple data
229 sources of soil profiles and remote sensing data (Hengl et al., 2017). The soil product underwent
230 rigorous quantitative evaluation using a cross-validation method, which ensures alignment with
231 established pedo-landscape features and provides spatial uncertainty to guide product users
232 (Poggio et al., 2021). Soilgrid v2 provides percent clay, percent sand, and soil organic matter for
233 six standard soil layers: 0–5 cm, 5–15 cm, 15–30 cm, 30–60 cm, 60–100 cm, and 100–200 cm.
234 The original SoilGrid version 2 data obtained from GEE were processed at 1 km resolution with
235 multiple layers using an area-weighted average method. To facilitate the demonstration, we
236 restructured the six soil layers vertically into ELM2's ten effective soil layers (0–1.8 cm, 1.8–4.5
237 cm, 4.5–9.1 cm, 9.1–16.6 cm, 16.6–28.9 cm, 28.9–49.3 cm, 49.3–82.9 cm, 82.9–138.3 cm, 138.3–
238 229.6 cm, and 229.6–380.2 cm) using the nearest neighboring method. It should be noted that the
239 lake module in ELM2 and CLM5 requires soil properties, but the Soilgrid v2 data may not provide

240 coverage over water surfaces. To address this, we utilized the nearest neighbor sampling method
241 to map the 1 km soil properties onto the terrestrial water surface.

242

243 **2.4 Topography-related parameters**

244 We employed the digital elevation from the Multi-Error-Removed Improved-Terrain DEM
245 (MERIT DEM, Yamazaki et al., 2019) to obtain topography-related parameters. The MERIT DEM
246 provides globally consistent elevation data at 90 m resolution, distinguished by its exceptional
247 vertical accuracy. This accuracy was rigorously validated against ICESat's lowest elevations in
248 both forested and non-forested regions and was further benchmarked using the UK's premium
249 airborne LiDAR DEM (Yamazaki et al., 2019). We first acquired the 1km elevation and standard
250 deviation of elevation using GEE based on the original 90 m elevation. Further, we calculated the
251 slope, aspect, sky view factor, and terrain configuration factor from the 1km elevation using the
252 parallel computing tool developed by Dozier (2022). The sky view factor represents the proportion
253 of visible sky limited by adjacent terrain, and the terrain configuration factor describes the
254 proportion of adjacent terrain which is visible to the ground target. Finally, to drive the
255 parameterization of sub-grid topographical effects on solar radiation (Hao et al., 2022) in ELM2,
256 we calculated the $\sin(\text{slope}) \cdot \sin(\text{aspect})$ and $\sin(\text{slope}) \cdot \cos(\text{aspect})$ for calculating the
257 local solar incident angle, and two normalized angle-related factors, the sky view factor, and terrain
258 configuration factor by $\cos(\text{slope})$. It is important to note that the standard deviation of elevation
259 calculated in this study is specific to the 1 km resolution simulation. For applications requiring
260 coarser resolutions (e.g., 0.5 degree), the standard deviation should be recalculated directly from
261 the 1 km elevation, rather than averaging from the 1k standard deviation of elevation.

262

263 **2.5 Comparison between new and existing land surface parameters**

264 In this study, since the data sources used to develop the 1k global land surface parameters have
265 already undergone rigorous validation, we do not perform additional evaluations against reference
266 datasets (e.g., observations). Instead, our focus is on comparing the newly developed 1k
267 parameters with those from K2012 and the ELM2/CLM5 default parameters. The K2012
268 parameters, obtained through personal communication (refer to the data availability section for
269 details). The ELM2/CLM5 default parameters were sourced from the CESM input data repository
270 (<https://svn-ccsm-inputdata.cgd.ucar.edu/trunk/inputdata/>). Given the different resolutions of
271 these datasets—our new parameters at 1km, K2012 at 0.05 degree, and ELM2/CLM5 defaults with
272 varying resolutions—we adapt our comparison at different resolutions for different variables.

273 For PFT parameters, we aggregated both the 1k new parameters and the 0.05-degree K2012 data
274 to the 0.5-degree resolution of the ELM2/CLM5 default. For non-vegetated land units (i.e., urban,
275 glacier, and lake), we upscaled the 1k new parameters to a 0.05-degree resolution to align with the
276 ELM2/CLM5 default. It is important to note that the urban parameter in K2012 is only available
277 for the northern hemisphere, due to limitations in data acquisition.

278 When comparing LAI, we aggregated the 1k new and K2012 LAI to 0.5-degree resolution,
279 matching the ELM2/CLM5 default LAI/SAI resolution. We excluded the comparison of SAI from
280 our analysis due to the limited availability of the global K2012 dataset, from which we only
281 acquired coverage for North America. We have not included a comparison of vegetation canopy
282 height (top and bottom parameters) in our study. This is because the K2012 dataset does not
283 contain these parameters, and the ELM2/CLM5 default parameters in the CESM input data
284 repository provide only tabular values for each PFT, rather than spatially variable canopy heights
285 for tree PFTs.

286 For soil and topography-related parameters, our comparison was limited to the 1k new parameters
287 and the ELM2/CLM5 default, as K2012 does not include these parameters. Specifically, for soil
288 comparisons, we aggregated the new 1k parameters to 0.083° resolution to match the ELM2/CLM5
289 default soil parameters. For topography, given that the ELM2/CLM5 default parameters is a
290 combination of 1k and 10 arc-minute data sources, we simplify the comparison by aggregating
291 both the new 1k parameters and ELM2/CLM5 default to 0.5-degree resolution, including elevation
292 and slope.

293

294 3. K-scale demonstration simulation over CONUS

295 3.1 Experiment design

296 To demonstrate the capability of 1 km datasets, we conducted ELM2 simulations over CONUS at
297 the resolution of 1 km, using the newly developed 1 km land surface parameters for 2010. We used
298 atmospheric forcing from the Global Soil Wetness Project Phase 3 (GSWP3; Kim, 2017) with a
299 spatial resolution of 0.5° to drive ELM. The spatial homogeneity of atmospheric forcings within
300 0.5° grid cell guarantees that the spatial variability of ELM simulated variables (e.g., latent heat)
301 within 0.5° grid cell is solely attributable to the heterogeneity of the 1 km land surface parameters.
302 There are approximately 12 million effective grids over CONUS. We ran ELM for five years
303 (2010–2014), and the last year’s simulation was used for analysis. We specifically analyzed the
304 annual mean of surface layer soil moisture (SM, m^3/m^3), latent heat (LH, W/m^2), emitted
305 longwave radiation (ELR, W/m^2), and absorbed shortwave radiation (ASR, W/m^2).

306 3.2 Spatial scaling analysis

307 We conducted a spatial scaling analysis following the method described in Vergopolan [et al.](#) (2022)
308 on the 1 km ELM simulation data to better understand how k-scale spatial heterogeneity in the
309 four ELM-simulated variables (mentioned in Section 3.1) induced only by spatial heterogeneity of
310 land surface parameters changes across spatial scales. First, we performed upscaling by averaging
311 the 1 km ($=1/120^\circ$) land surface parameters and the four ELM-simulated variables to coarser
312 spatial scales, λ_{scale} of $1/60^\circ$, $1/40^\circ$, $1/30^\circ$, $1/24^\circ$, $1/20^\circ$, and $1/10^\circ$, and calculated the spatial
313 standard deviation (σ_{scale}) within each $0.5^\circ \times 0.5^\circ$ box at each spatial scale (Table 2). Second, we
314 quantified the changes in spatial variability at different spatial scales compared to the original 1 km
315 resolution by calculating the ratio of σ_{scale} to $\sigma_{1 km}$. Third, we fitted a $\log\left(\frac{\sigma_{scale}}{\sigma_{1 km}}\right) \propto$
316 $\beta \times \log\left(\frac{\lambda_{scale}}{\lambda_{1 km}}\right)$ relationship, where β is an indicator to quantify data spatial variability persistence

317 across scales (Hu et al., 1997). A more negative β indicates a larger dependency of data spatial
 318 variability on spatial scales, resulting in a higher information loss, denoted as $\gamma_{scale} =$
 319 $(1 - \sigma_{scale} / \sigma_{1\text{ km}}) \times 100\%$. In this study, we focus on information loss at a 12 km scale, denoted
 320 as $\gamma_{12\text{ km}}$. For simplicity in subsequent discussion, $\gamma_{12\text{ km}}$ will be referred to as γ in the results
 321 section. Given the possibility that β may not demonstrate significant temporal variation (Mälicke
 322 et al., 2020), and considering that our scaling analysis is intended for demonstration purposes, our
 323 spatial scaling analysis is based on the annual mean of ELM2 simulations.

324 [It is crucial to clarify that the upscaled 1 km simulation results in the spatial scaling analysis are](#)
 325 [not equivalent to the results obtained from a coarse resolution ELM conducted using upscaled](#)
 326 [parameters. The spatial scaling analysis is intended to emphasize the value of high-resolution](#)
 327 [modeling in capturing fine-scale spatial variabilities, and to highlight the contributions of high-](#)
 328 [resolution land surface parameters on the simulated variables.](#)

329 Table 2. Spatial resolution and pixel number at different spatial scales.

$\lambda_{scale} / \lambda_{1\text{ km}}$	1	2	3	4	5	6	12
Spatial resolution	1km (1/120°)	2km (1/60°)	3km (1/40°)	4km (1/30°)	5km (1/24°)	6km (1/20°)	12km (1/10°)
Pixel number within 0.5° × 0.5° box	60 × 60	30 × 30	20 × 20	15 × 15	12 × 12	10 × 10	5 × 5

330

331 3.3 Attribution analysis utilizing XML methods

332 We conducted additional analysis to determine the primary land surface parameters that influence
 333 the spatial scaling of ELM simulations. We employed XML methods, specifically the eXtreme
 334 Gradient Boosting (XGBoost; Chen and Guestrin, 2016) machine learning algorithm and the game
 335 theoretic approach SHapley Additive exPlanations (SHAP; Lundberg and Lee, 2017; Lundberg et
 336 al., 2018, 2020). XML methods were utilized to assess the influence of land surface parameters on
 337 the spatial variability and information loss of ELM2 simulations across the CONUS. Taking spatial

338 variability as an example, we first computed the standard deviation (σ) within each $0.5^\circ \times 0.5^\circ$ grid
339 for both 1 km resolution land surface parameters and simulations. Then, we train a machine
340 learning model to predict the spatial variability of each simulated variable (i.e., SM, LH, ELR,
341 ASR). We used the spatial variability (i.e., σ) and mean (μ) of the land surface parameters and μ
342 of precipitation and temperature as predictor variables, and the simulated variable's σ as the target
343 variable. After training the machine learning model, we used SHAP to quantify the relative
344 importance and determine which factors were most important in driving the spatial variability of
345 the simulations. Similarly, we used this approach to identify the most critical drivers of information
346 loss.

347 **3.4 Reference datasets for evaluating ELM simulation**

348 We also performed a comparison of all four ELM-simulated variables against reference datasets.
349 It is important to note that we used the default model parameters and did not perform any
350 calibration (see discussions for details). For reference datasets, soil moisture was obtained from
351 the Global Land Evaporation Amsterdam Model (GLEAM; Martens et al., 2017), latent heat flux
352 data was from the MODIS product (Running et al., 2021), and both ELR and ASR data were
353 processed from the land component of the fifth generation of European ReAnalysis (ERA5_Land;
354 Muñoz-Sabater et al., 2021). For the soil moisture evaluation, we compared the surface layer soil
355 moisture from GLEAM (10 cm depth) with the weighted average of the first four-layer soil
356 moisture from ELM (about 11 cm depth). To ensure comparability, we unified the spatial
357 resolution of both reference datasets and ELM simulations to a 0.5-degree resolution and focused
358 our analysis on the annual mean data for 2014.

359

360

361 **4. Results**

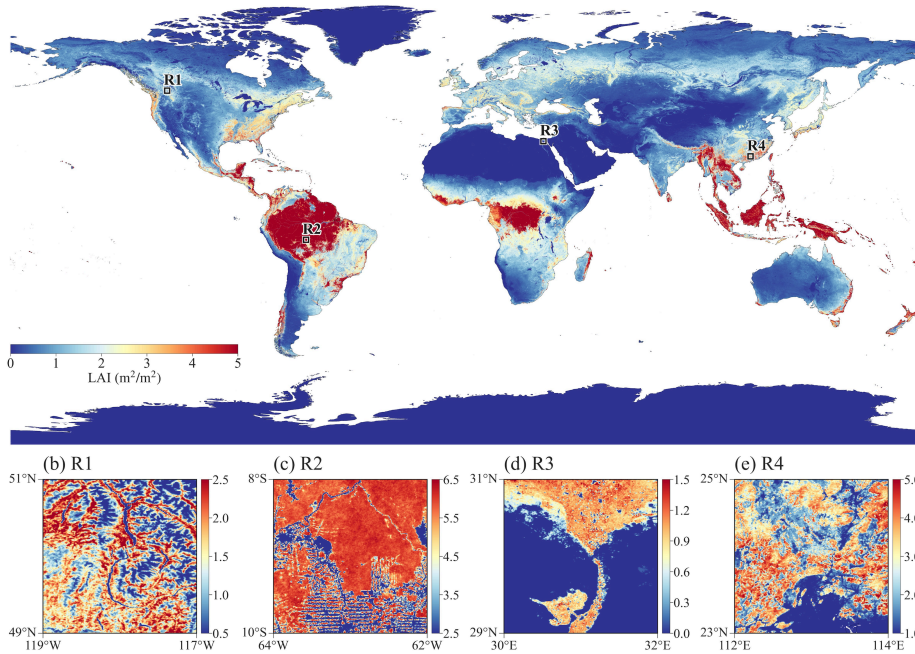
362 **4.1 Demonstration of the global 1km land surface parameters**

Deleted: 3

363 LAI generally shows high values in humid and warm regions, such as tropical rainforests,
364 southeastern US, and southern Asia, and low values over arid or cold regions, such as central
365 Australia, southwestern US, Middle East, Central Asia, and northern Canada (Figure 1a). At high
366 resolution, the LAI dataset clearly reflects the detailed heterogeneity of vegetation distributions.
367 In subregion R1 (Figure 1b), a relatively small LAI is distributed over mountain ridges and zero
368 LAI over water surfaces (e.g., lakes). In subregion R2 (Figure 1c), the LAI pattern shows a large
369 proportion of forest fragmentation caused by deforestation. In subregion R3 (Figure 1d), the LAI
370 shows the distribution of agricultural land along with the river, river mouth, and lakes under an
371 arid climate. R4 shows how urbanization affects vegetation distributions (Figure 1e).

372 Figure 2 demonstrates the distribution of plant functional types and other non-vegetation land units.
373 High-resolution LULC types over multiple years can benefit studies related to LULC changes like
374 urbanization and deforestation. Canopy height generally follows a similar spatial pattern with LAI,
375 with high values in humid and warm regions and low values over arid or cold regions (Figure 3a).
376 The percent clay shows high values over Southeast Asia, India, central Africa, and southeast South
377 America, and low content over North Europe, South Africa and Alaska (Figure 3b). The
378 topography factors follow the elevation patterns (Figures 3c and 3d), where there are large slopes
379 and standard deviation of elevation over mountainous regions, such as the Rocky Mountains in
380 North America, the Himalayas Mountains in Asia, and Andes Mountains in South America.

(a) LAI (m^2/m^2)



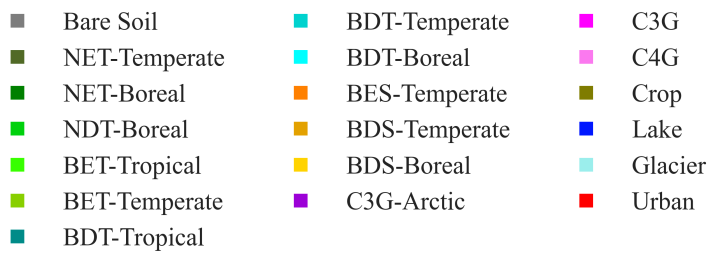
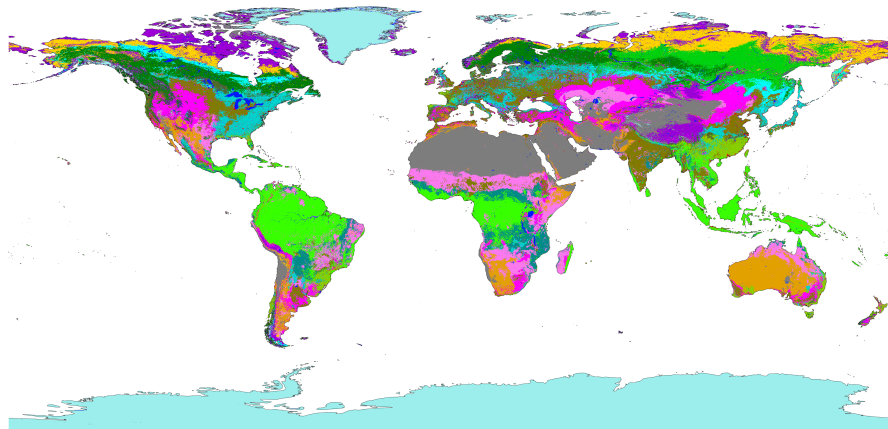
382

383 Figure 1. The spatial pattern of LAI (annual mean in 2010) over (a) global land and (b)~(e) four

384 subregions R1~R4 within 2-degree boxes marked in (a). Subregions R1~R4 represent

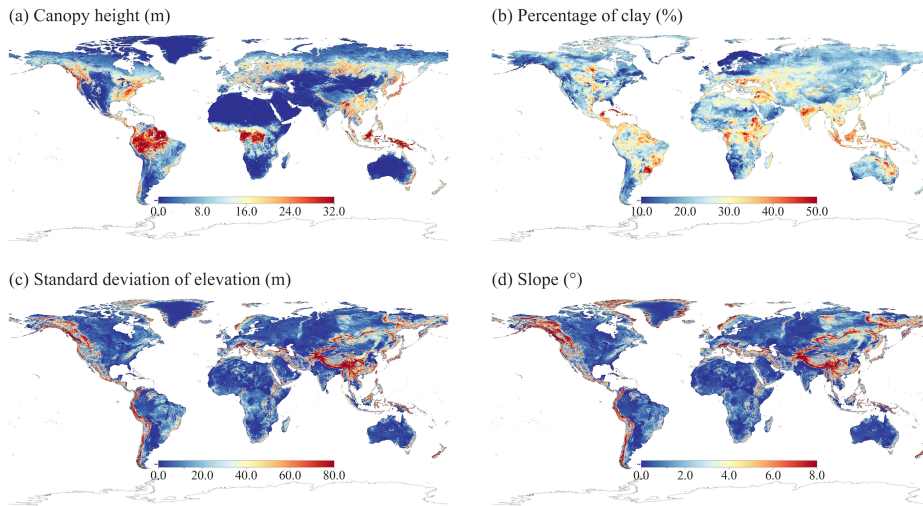
385 topography, deforestation, irrigations, and urbanization effects on LAI.

386



387

388 Figure 2. Global LULC distribution in year 2010. PFT abbreviations include: Bare Soil, Needleleaf
 389 Evergreen Trees in temperate (NET-Temperate) and boreal (NET-Boreal) regions, Needleleaf
 390 Deciduous Trees in boreal regions (NDT-Boreal), Broadleaf Evergreen Trees in tropical (BET-
 391 Tropical) and temperate (BET-Temperate) regions, Broadleaf Deciduous Trees in tropical (BDT-
 392 Tropical), temperate (BDT-Temperate), and boreal (BDT-Boreal) regions, Broadleaf Evergreen
 393 Shrubs in temperate regions (BES-Temperate), Deciduous Shrubs in temperate (BDS-Temperate)
 394 and boreal (BDS-Boreal) regions, C3 Grass in arctic (C3G-Arctic) and general (C3G) varieties,
 395 C4 Grass (C4G), Crop, Lake, Glacier, and Urban.



396
 397 Figure 3. Demonstration of global 1km datasets (a) Canopy top height, (b) percent clay, (c)
 398 standard deviation of elevation, and (d) slope.

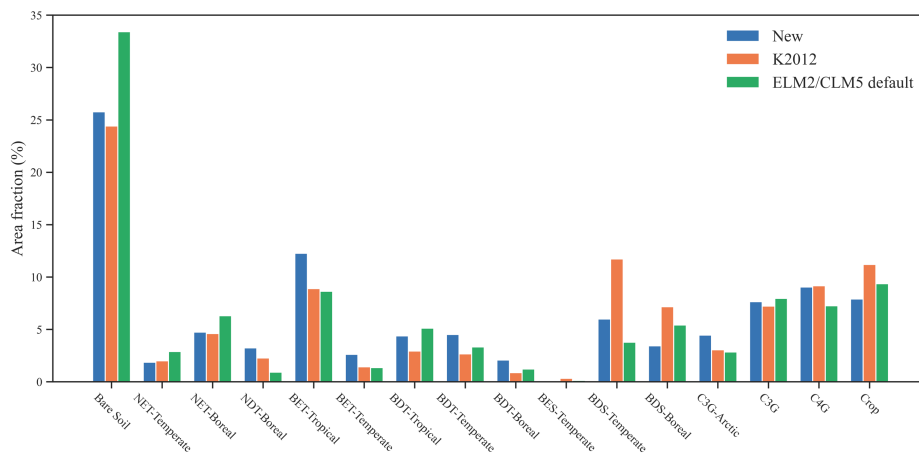
399

400 **4.2 Comparison between new and existing land surface parameters**

Deleted: 3

401 The global distributions of different PFTs show varying degrees of difference when comparing the
 402 new parameters with the K2012 and ELM2/CLM5 default parameters (Figure 4 and
 403 Supplementary Figures S1 to S16). Predominant types such as bare soil, BET-Tropical tree, C3
 404 and C4 grass, and crop are found consistently across all datasets. Notable differences include less
 405 bare soil in the new parameters and K2012 compared to ELM2/CLM5 default, especially in high-
 406 latitude North America, western US, South Africa, Central Asia, and Central Australia (Figure S1).
 407 While the new NDT PFT shows larger coverage in Siberia than K2012 and ELM2/CLM5 (Figure
 408 S4), BET-Tropical PFT is more prevalent in the new parameters across Central and South America
 409 (Figure S5). BET-Temperate PFT has greater area coverage in southern China in the new
 410 parameters (Figure S6). For BDT-Tropical, BDT-Temperate, and BDT-Boreal PFTs, both the new

412 and ELM2/CLM5 default parameters surpass K2012 data in coverage (Figures S7 to S9). The
 413 coverage of new BDS-Temperate PFT is smaller than K2012 but larger than ELM2/CLM5 default
 414 (Figure S11), and the new BDS-Boreal PFT is less extensive in the boreal northern hemisphere
 415 compared to both K2012 and ELM2/CLM5 defaults (Figure S12). The C3-Arctic PFT shows
 416 larger areas in the new parameters, particularly in northern Canada, with the new C4 grass PFT
 417 being similar to that of K2012 and larger than ELM2/CLM5 C4 grass. Crop PFT is less extensive
 418 in the new parameters, particularly in Southeastern China, Europe, South America, Africa, and
 419 Australia.

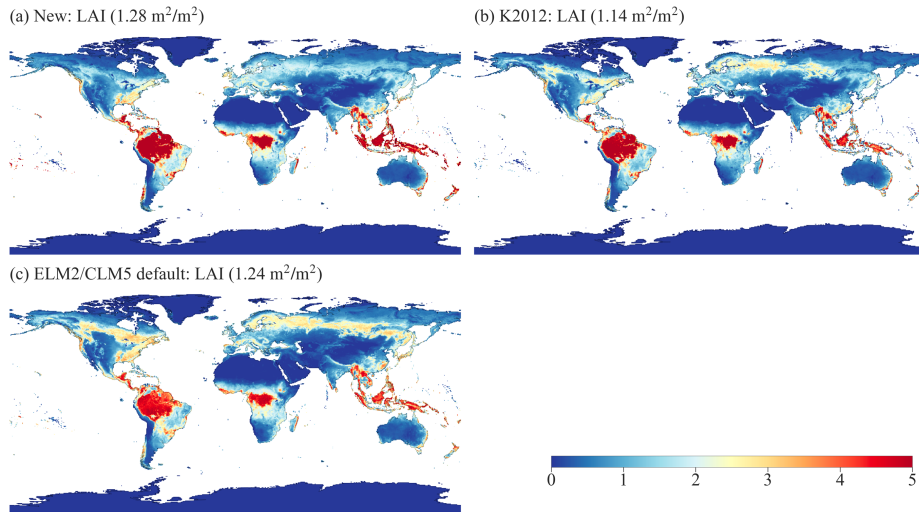


420
 421 Figure 4. The global average area fractions of PFTs for three land surface parameter datasets. PFT
 422 abbreviations used on the X-axis are displayed in Figure 2.

423
 424 The global distributions of non-vegetated land covers of lake, glacier and urban areas vary among
 425 the datasets (Figure S17–S19). The new dataset shows slightly less lake coverage than K2012, but
 426 both are smaller than ELM2/CLM5 default, particularly in high-latitude North America (Figure
 427 S17). Glacier coverage in the new parameter is around 0.7% smaller than K2012, with noticeable

428 differences in the Arctic North America, while ELM2/CLM5 default shows more extensive glacier
429 coverage in Antarctica (Figure S18). Regarding urban areas, K2012 has the smallest urban
430 coverage in the Northern Hemisphere compared to both the new dataset and ELM2/CLM5 default
431 (Figure S19). Meanwhile, ELM2/CLM5 default exhibits more expansive urban areas in India and
432 China than the new dataset and K2012.

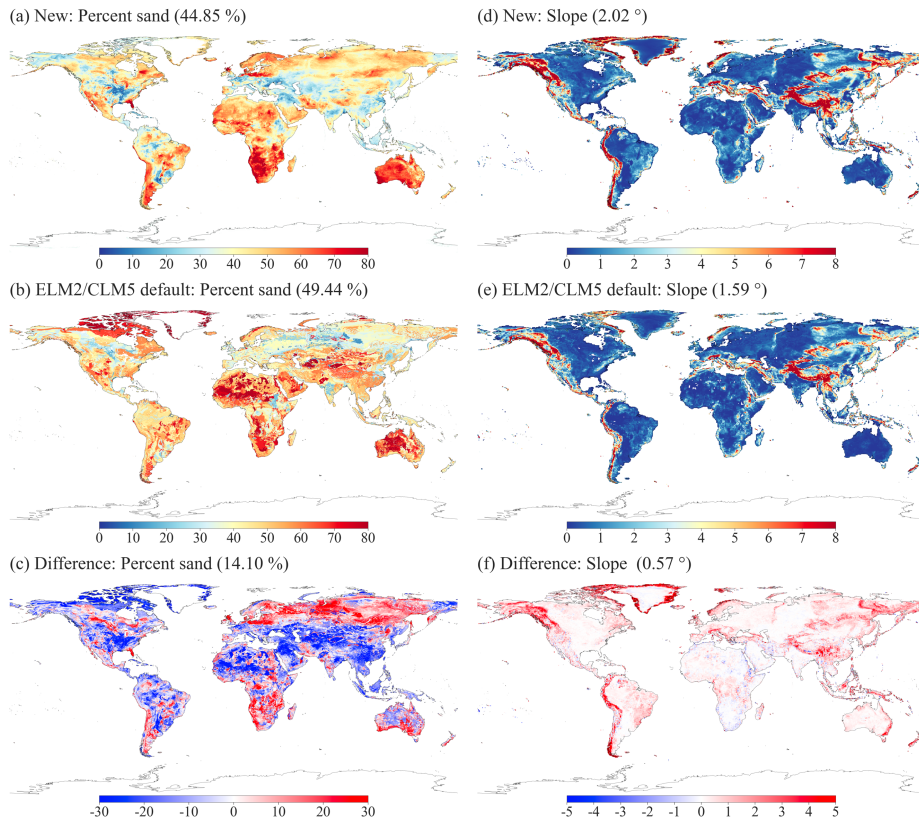
433
434 The global annual mean LAI exhibits similar spatial patterns among the new parameter, K2012,
435 and ELM2/CLM5 (Figure 5). The overall global mean LAI for the new parameter ($1.28 \text{ m}^2/\text{m}^2$) is
436 slightly higher than that of K2012 ($1.14 \text{ m}^2/\text{m}^2$) and the ELM2/CLM5 default data ($1.24 \text{ m}^2/\text{m}^2$).
437 In terms of spatial pattern, the new LAI, relative to K2012 (Figure S20a), shows lower values in
438 the NET-Boreal PFT over the northern hemisphere, but higher values in the BET-Tropical PFT
439 over the tropics. Similarly, compared with the ELM2/CLM5 default LAI (Figure S20b), the new
440 LAI also presents smaller values in both the NET-Boreal and NDT PFTs over the northern
441 hemisphere, but larger values in the BET-Tropical PFT regions.



442
 443 Figure 5. Comparison of global annual mean LAI for (a) new, (b) K2012, and (c) ELM2/CLM5
 444 default parameters. The global average is indicated in the subplot title.

445
 446 Soil parameters exhibit significant differences between the new and ELM2/CLM5 default datasets
 447 (Figures 6a-bc, S21, and S22). The global mean absolute differences between the new and
 448 ELM2/CLM5 default for percent sand, percent clay, and organic matter are 14.1%, 8.1%, and 30.5
 449 kg/m³, respectively. Generally, the new soil parameters are spatially distributed more smoothly
 450 than those from ELM2/CLM5 with more patchy patterns (Figure 6a vs. 6b). Specifically, the new
 451 percent sand is higher in regions like Europe, Siberia, South Africa, and Southern Australia, but
 452 lower in areas such as the Lower Mississippi River Basin, North Africa, and Central and
 453 Southeastern Asia (Figure 6c). The new percent clay shows larger values in the Western US, North
 454 Africa, Central Asia, and Australia, but smaller values in Alaska and Eastern Europe (Figure S21).

455 For organic matter, the new parameter indicates smaller values in the Northern Hemisphere but
456 larger values in other global regions compared to the ELM2/CLM5 default (Figure S22).
457 Topography-related parameters exhibit broadly similar spatial patterns but with notable
458 differences between the new and ELM2/CLM5 default parameters, as seen in Figures 6d-6f and
459 S23. The new slope parameter generally shows a larger slope relative to the ELM2/CLM5 default,
460 particularly in mountainous regions (Figure 6f). This could be attributed to the new 1 km slope
461 being calculated from a finer 90 m resolution elevation. Differences in elevation between the new
462 and ELM2/CLM5 parameters are more pronounced in areas such as various mountainous regions,
463 Greenland, the Amazon Basin, the Tibetan Plateau, and Australia (Figure S23).



464
 465 Figure 6. Comparisons of percent sand and slope. (a) new and (b) ELM2/CLM5 default percent
 466 sand, along with (c) their difference (new – ELM2/CLM5 default) for percent sand; (d) new, (e)
 467 ELM2/CLM5 default, and (f) their difference for slope. The global average is shown in the subplot
 468 titles, with the global average of the absolute difference provided for (c) and (f).

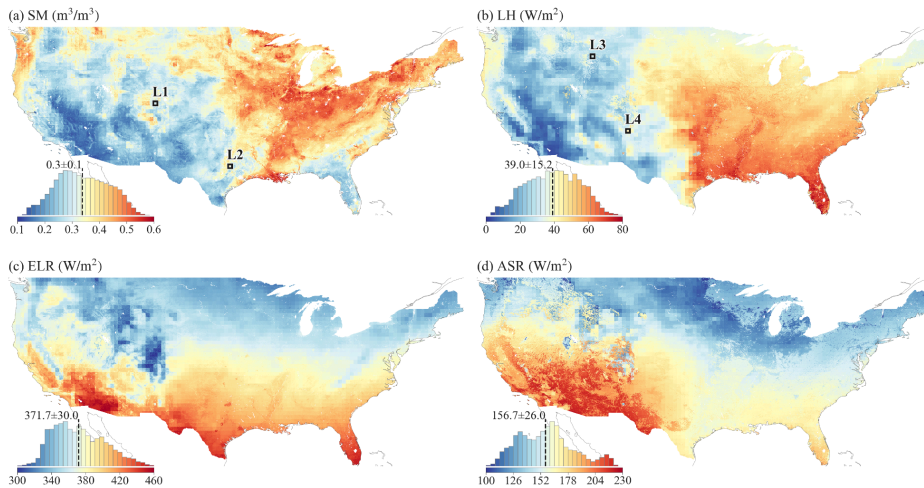
469

470 **4.3 Demonstration 1km simulation over CONUS**

471 ELM simulations at a 1 km resolution display significant spatial heterogeneity over CONUS
 472 (Figure 7). The values of SM, LH, ELR, and ASR across CONUS follow approximately normal

Deleted: 3

474 distributions, with averages of $0.3 \text{ m}^3/\text{m}^3$, $39.0 \text{ W}/\text{m}^2$, $371.7 \text{ W}/\text{m}^2$, $156.7 \text{ W}/\text{m}^2$, respectively (as
 475 shown in the histogram plots in Figure 7). SM shows drier conditions over the West and Southwest
 476 and wetter conditions over the Midwest, Corn Belt, Mississippi River basin, and Northeast (Figure
 477 7a). LH shows high values over the central and southeast, and lower values over the west and
 478 southwest (Figure 7b). The ELR generally shows higher values over regions with high surface
 479 temperature in the south (Figure 7c). The ASR shows higher values over the southwestern regions
 480 determined by incoming solar radiation and albedo (Figure 7d). Despite the high-resolution
 481 heterogeneity shown at 1 km resolution, we can still see the spatial patterns distinguished at coarse
 482 resolution, i.e., $0.5^\circ \times 0.5^\circ$. These coarser footprints are from the GSWP3 atmospheric forcing with
 483 0.5° resolution. As concluded by Li et al. (2022), atmospheric forcing is one primary heterogeneity
 484 source for land surface modeling. Therefore, k-scale atmospheric forcing needs to be developed to
 485 further advance k-scale offline land surface modeling.



486
 487 Figure 7. The annual mean of 1 km simulations of (a) SM, (b) LH, (c) ELR, and (d) ASR over
 488 CONUS. The $0.5^\circ \times 0.5^\circ$ boxes marked as L1, L2, L3, and L4 in (a) and (b) are selected to

Deleted:)

490 demonstrate the spatial scaling analysis. The inserted histogram plot illustrates the distribution of
491 ELM2 simulations.

492

493 **4.4 Demonstration of spatial scaling across scales**

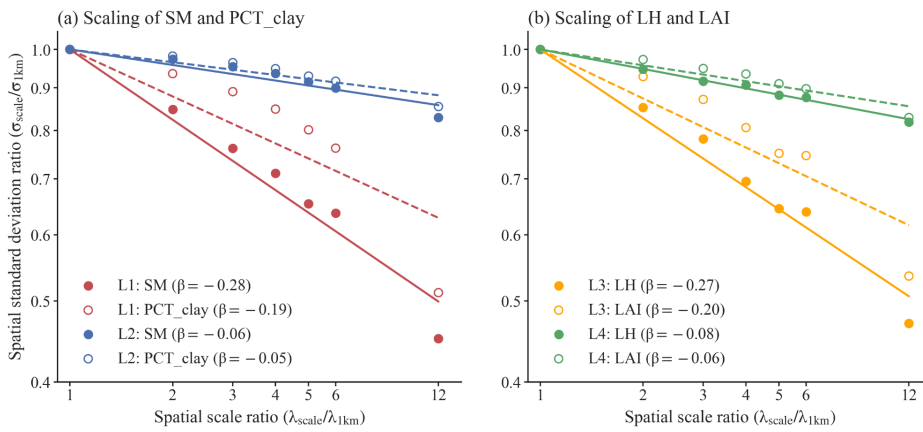
Deleted: 3

494 We next demonstrate the relationships between spatial variabilities and spatial scales for SM and
495 LH. Four locations (in Figures 4a and 4b) are specifically chosen to showcase varying levels of
496 spatial information loss: L1 and L3 demonstrate a relatively large loss for SM and LH, respectively,
497 while L2 and L4 represent a relatively small loss for SM and LH, respectively.

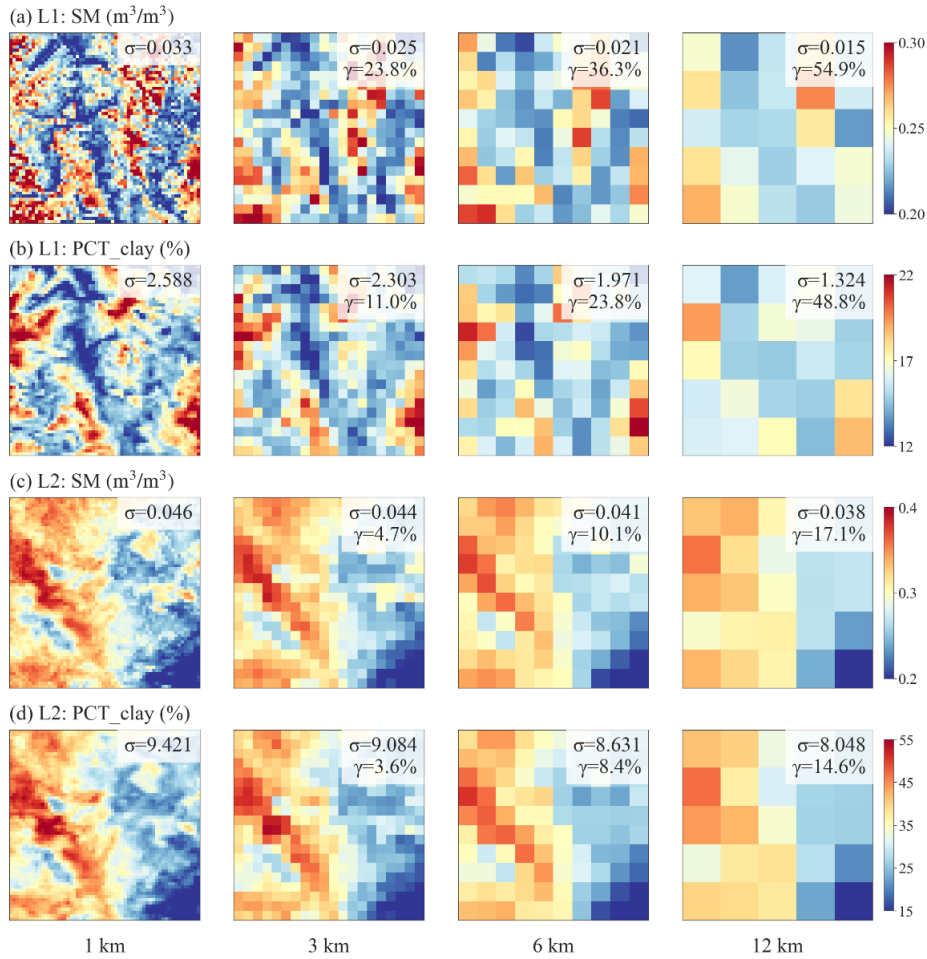
498 At location L1 (Figure 8a), when the 1 km simulation is upscaled to coarser resolutions (i.e., larger
499 spatial scale ratios), the spatial variability of SM decreases, resulting in a negative slope of β . As
500 shown in Figure 9a, compared to the original 1 km resolution, the information loss γ reaches up to
501 54.9% at the 12 km spatial scale. The spatial pattern of SM is consistent with the spatial pattern of
502 percent clay (Figures 6a vs. 6b and 6c vs. 6d), indicating that soil texture contributes significantly
503 to the spatial variability of SM. However, SM has a more negative β than the percent clay ($\beta = -$
504 0.28 vs. -0.19 at L1, as shown in Figure 8a), suggesting that SM variability is amplified likely by
505 other processes that are also influenced by soil texture. In contrast to location L1, location L2
506 exhibits less negative β values for both SM and percent clay, suggesting that their spatial
507 variabilities exhibit less scale dependence (Figures 5a, 6c, and 6d). Both SM and percent clay at
508 location L2 approximately maintain their spatial patterns of high values in the west and low values
509 in the east across spatial scales (Figures 6c and 6d).

510 For LH, there is a more negative β value at location L3 than at location L4 ($\beta = -0.27$ at L3 vs. $-$
511 0.08 at L4, as shown in Figure 8b), which indicates a larger decrease of spatial variability across
512 spatial scales and lower variability persistence at location L3 than location L4 (Figure 10). The

514 spatial pattern of LH is consistent with the spatial pattern of LAI (Figures 7a vs. 7b and 7c vs. 7d)
 515 at different spatial scales, suggesting that vegetation plays a significant role in the spatial
 516 variability of LH. Similar to comparison between SM and soil texture, LH has a more negative β
 517 than LAI (Figure 8b).

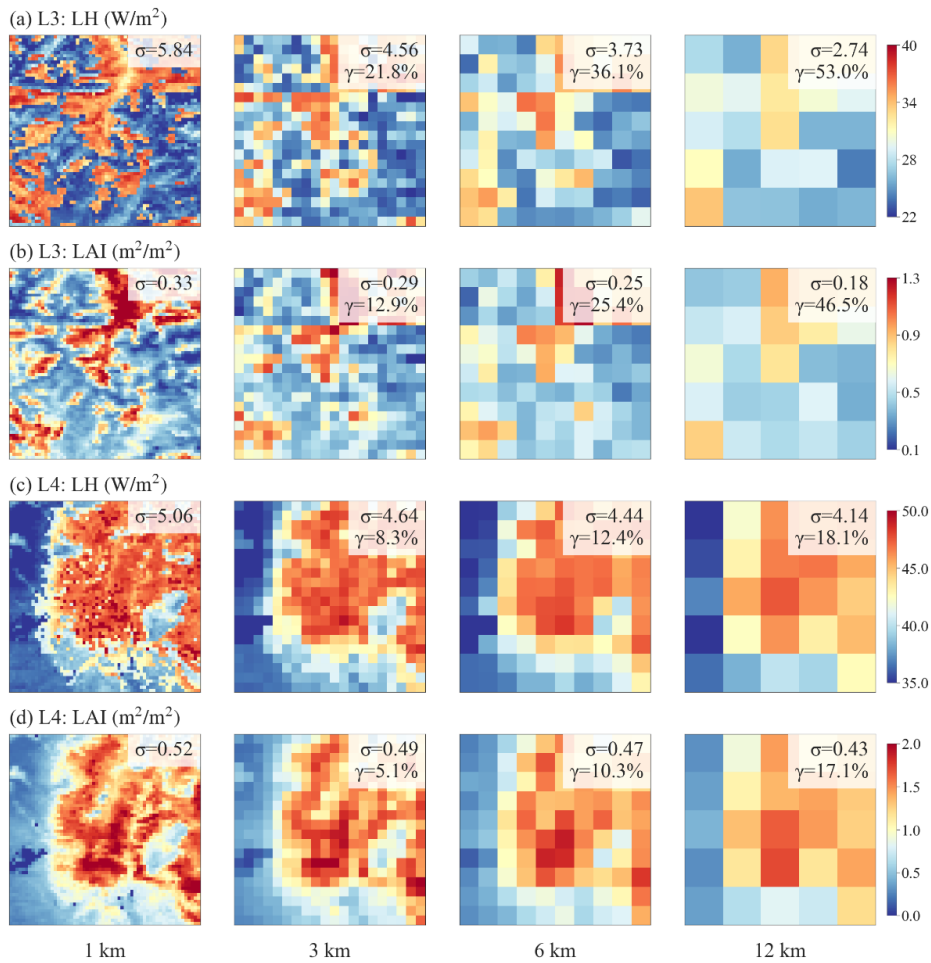


518 Figure 8. The scaling of spatial variabilities for (a) SM and percent clay, and (b) LH and LAI. Both
 519 the x-axis and y-axis are in logarithmic scale. The slope of the linear regression line, β , quantifies
 520 the strength of the negative relationship between spatial scale and spatial variability. A more
 521 negative β value indicates a higher spatial-scale dependency and increased information loss at
 522 coarser spatial scales. Four $0.5^\circ \times 0.5^\circ$ boxes (displayed in Figure 7), namely L1 to L4, are chosen
 523 to contrast larger and smaller negative β values for SM and percent clay (L1 and L2) and for LH
 524 and LAI (L3 and L4).
 525



526

527 Figure 9. Comparison of SM and percent clay across spatial scales at locations L1 and L2
 528 highlighted in Figure 7. Each subplot displays the spatial patterns of SM or percent clay within a
 529 $0.5^\circ \times 0.5^\circ$ box, with the σ and γ presented in the legend.



530

531 Figure 10. Similar to Figure 9, but for LH and LAI at locations L3 and L4.

4.5 The spatial variability of water and energy simulations and their drivers

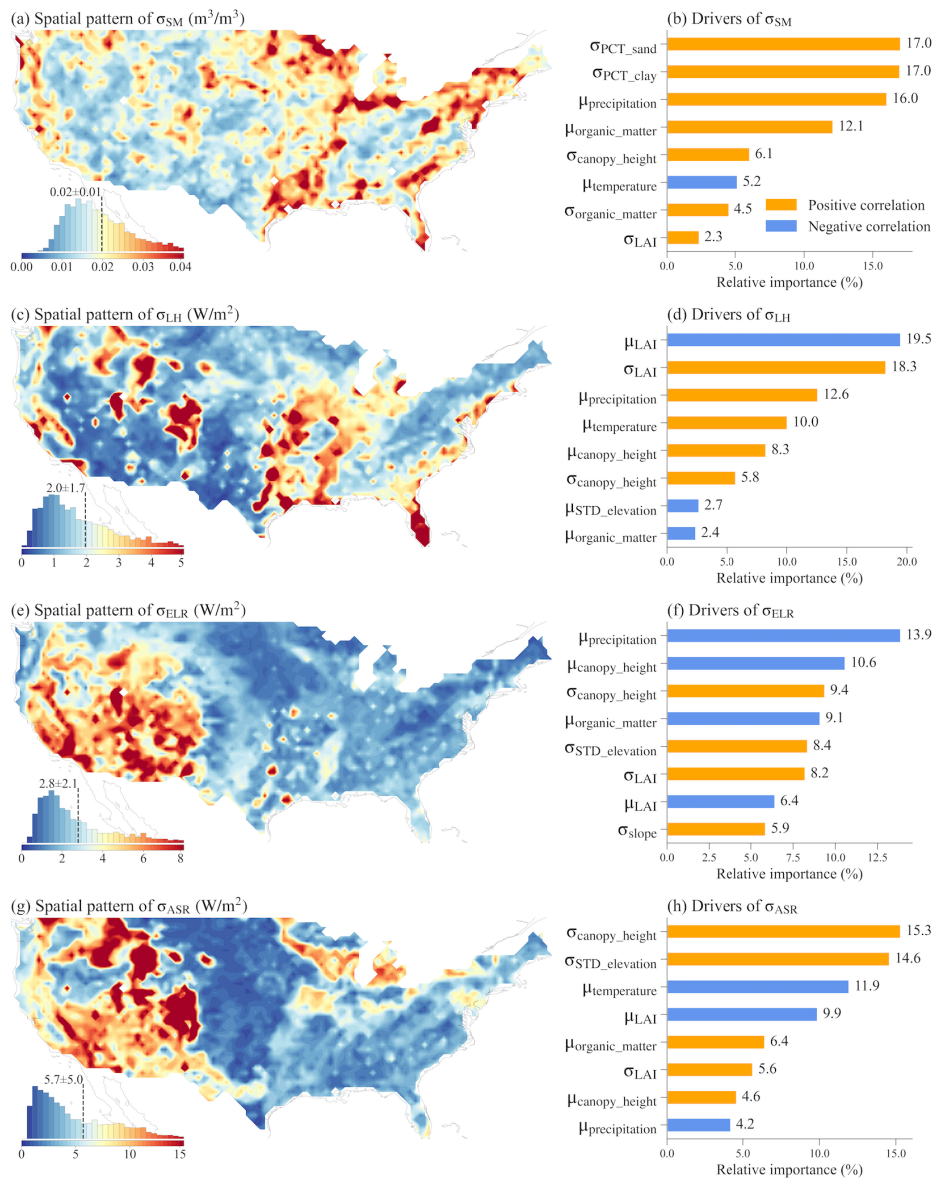
Deleted: 3

We quantified the spatial variability simulated at 1 km resolution using σ within each $0.5^\circ \times 0.5^\circ$ box across CONUS. Four ML models were built to explore the spatial relationships between σ and its potential drivers including σ of the land surface parameters and the temperature and precipitation averaged over the grid box. Overall, the ML models performed well in predicting the σ of the simulated variables, with small root mean square error (RMSE) and large R^2 (see Figure S24). SM shows larger spatial variability in the US Southern Coastal Plain, lower Mississippi River, Northeast, Southeast, and regions around the Great Lake (Figure 11a), which is roughly consistent with the spatial heterogeneity of the high-resolution SM simulation in Vergopolan et al. (2022). Based on the SHAP method, the spatial variability of SM across CONUS is driven by various factors, mainly including the spatial variabilities of percent sand and percent clay, mean precipitation, the σ and μ of soil organic matter, the σ of canopy height, and mean temperature (Figure 11b). Mean precipitation and temperature reflect climate conditions (Figure S26), which are related to the water supply and water demand of soil water content. The spatial heterogeneity of soil properties, such as texture and organic matter content, affects soil hydraulic properties and generate more spatially variable soil water content. Vegetation characteristics, such as canopy height and LAI, could influence SM spatial variability through their effect on roughness length and rooting depth.

The spatial variability of LH is large in the southeastern, central, and western mountainous regions of the US (Figure 11c). Vegetation properties and climate conditions mainly drive the variability of LH (Figure 11d). The μ and σ of LAI can affect transpiration and soil evaporation, while canopy height can influence surface roughness length and, in turn, evapotranspiration. Mean precipitation

555 and temperature reflect the overall climate conditions related to the water and energy available for
556 latent heat.

557 ELR and ASR exhibit large spatial variability mainly over the western US, with ASR additionally
558 showing significant spatial variability across the Northern US (Figures 8e and 8g). This variability
559 is primarily driven by climate conditions such as mean precipitation and temperature, topographic
560 features such as standard deviation of elevation and slope, and vegetation properties including LAI
561 and canopy height (Figures 8f and 8h). These factors are related to the radiation input and surface
562 properties, such as albedo and roughness length, which impact the energy cycles and availability
563 of ELR and ASR.



564
 565 Figure 11. The spatial variability over each $0.5^\circ \times 0.5^\circ$ grid cell (left plots) and the top eight most
 566 important drivers (right plots) of the spatial variability for SM, LH, ELR, and ASR. The inserted

567 histogram plot illustrates the probability distribution of the spatial variability across CONUS. The
568 relative importance of each variable in determining the spatial variability is calculated as the ratio
569 of the mean |SHAP value| of the variable to the sum of the mean |SHAP value| of all variables.
570 Therefore, the sum of the relative importance of all variables is 100%.

571

572 **4.6 The information loss of water and energy simulations and their drivers**

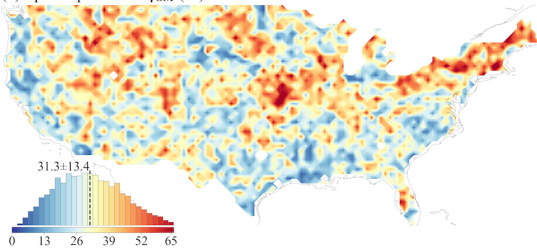
Deleted: 3

573 We also evaluated the information loss in simulations when upscaling from 1 km to 12 km
574 resolution and analyzed the drivers of their spatial patterns over CONUS. Four ML models were
575 built to explore the relationships between the γ of the simulations and its drivers including the γ of
576 the land surface parameters and the mean temperature and precipitation averaged over the $0.5^\circ \times$
577 0.5° box. These ML models performed well in predicting the simulations' γ , with small RMSE and
578 large R^2 (Figure S25).

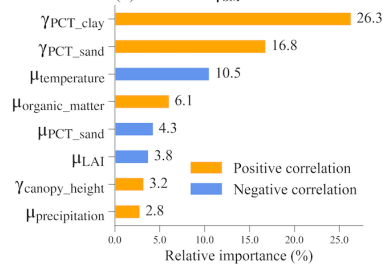
579 Significant information loss ranging from 31% to 54% with maximum values exceeding 90% is
580 observed for SM, LH, ELR, and ASR simulations (Figure 12). Their spatial patterns and drivers
581 show distinct variations. γ_{SM} is primarily driven by the information loss of percent clay and sand,
582 mean soil organic matter, and mean temperature, which affects the soil hydraulic properties and
583 soil water balance (Figures 9a and 9b). γ_{LH} displays high values in the eastern US and low values
584 in the western US (Figure 12c). It is primarily contributed by the information loss of vegetation
585 properties such as LAI and canopy height, and mean LAI, which influences the partitioning of LH
586 and sensible heat, and the partitioning of transpiration and evaporation (Figure 12d). γ_{ELR} exhibits
587 high values in the central and eastern US, particularly in the northeastern US, while γ_{ASR} has high
588 values almost all over the US, especially in the eastern regions (Figures 9e and 9g). γ_{ELR} and γ_{ASR}
589 are largely driven by vegetation properties such as LAI and canopy height, which are associated

591 with energy processes such as albedo (Figures 9f and 9h). Additionally, topography factors of
592 standard deviation of elevation and slope also slightly contribute to γ_{ASR} .

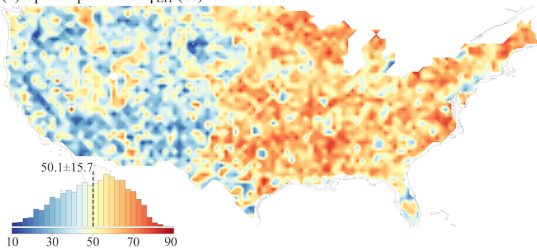
(a) Spatial pattern of γ_{SM} (%)



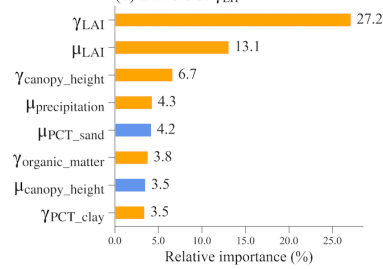
(b) Drivers of γ_{SM}



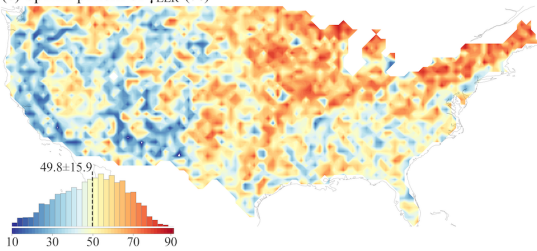
(c) Spatial pattern of γ_{LH} (%)



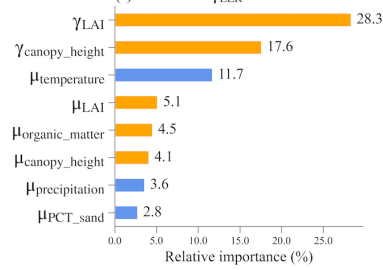
(d) Drivers of γ_{LH}



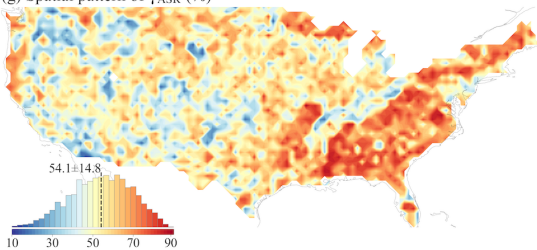
(e) Spatial pattern of γ_{ELR} (%)



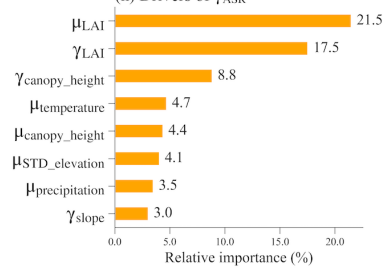
(f) Drivers of γ_{ELR}



(g) Spatial pattern of γ_{ASR} (%)



(h) Drivers of γ_{ASR}

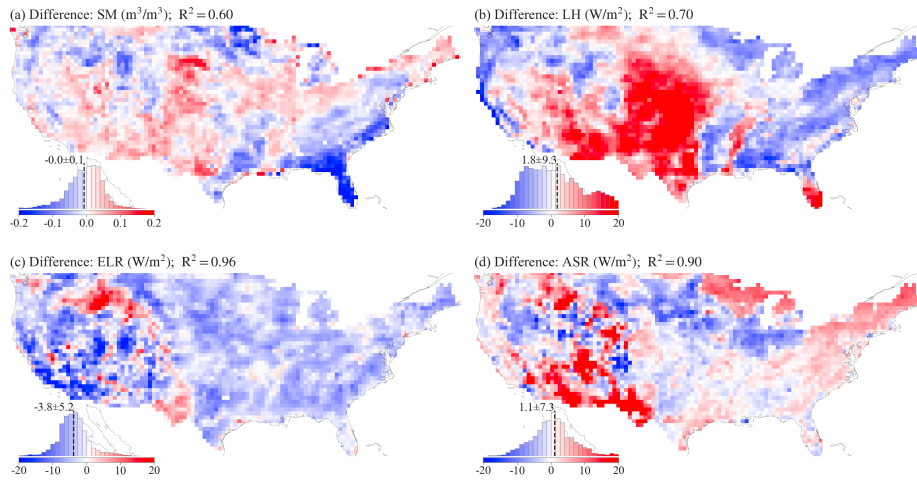


593

594 Figure 12. Same to Figure 11 but for information loss.

595 **4.7 Comparison of ELM simulation against reference data**

596 The average spatial biases between ELM and reference datasets across CONUS are relatively small,
597 with SM bias at -0.01 m³/m³, LH bias at 1.8 W/m², ELR bias at -3.8 W/m², and ASR bias at 1.1
598 W/m² (Figure 13 and Figure S27). The correlation coefficient (R²) between ELM and reference
599 datasets was relatively high at 0.60 (for SM), 0.70 (for LH), 0.96 (for ELR), and 0.90 (for ASR).
600 However, the spatial distribution of these biases exhibits variability, with some areas showing
601 more pronounced biases than others. Specifically, in comparison with GLEAM SM, ELM tends
602 to underestimate SM in the southeastern Texas and across the eastern and southeastern CONUS,
603 while it overestimates SM in the western, central, and southwestern CONUS, including the central
604 eastern US which are primarily agricultural areas. For LH, ELM simulates higher values than the
605 MODIS LH dataset in the western and central US and Florida, but lower values in regions such as
606 the eastern and northeastern CONUS, the western US coastal areas, and the Pacific Northwest.
607 Regarding radiation variables, ELM generally underestimates ELR across nearly all of CONUS
608 and tends to overestimate ASR, particularly in the southwestern, southern, eastern, northeastern,
609 and northern regions of CONUS.



610
 611 [Figure 13. Annual mean bias between ELM-simulated variables and reference datasets over](#)
 612 [CONUS: \(a\) SM, \(b\) LH, \(c\) ELR, and \(d\) ASR. The negative values indicate lower ELM values](#)
 613 [compared to the reference data. The inserted histogram plot illustrates the distribution of grid](#)
 614 [values. For spatial patterns of the reference datasets, refer to Figure S27. The correlation](#)
 615 [coefficient \(\$R^2\$ \) between the ELM simulation and the reference dataset is calculated and displayed](#)
 616 [in the title of each subplot.”](#)

617 **5. Discussion**

618 The development of new 1 km land surface parameter datasets in this study marks a substantial
619 improvement over commonly used land surface parameters such as CLM5 and K2012, leveraging
620 the latest high-resolution data sources with rigorous validation, including MODIS PFTs, enhanced
621 LAI and canopy height, soil properties, and topography factors. When compared with K2012 and
622 ELM2/CLM5 default datasets, the new 1k parameters exhibit notable differences, suggesting
623 potential improvement due to the use of more advanced data sources. Distinct features of the new
624 parameters include a reduction in bare soil compared to ELM2/CLM5, especially in regions like
625 North America and Central Asia, and diverse coverage of specific PFTs such as NDT and BET-
626 Tropical in areas like Siberia and South America. The LAI of the new parameters diverges from
627 K2012 and ELM2/CLM5, showing lower values in NET-Boreal PFT of the northern hemisphere
628 but higher BET-Tropical PFT in the tropics. The soil parameters, particularly in regions like
629 Europe, Central Asia, and the Western US, show significant differences between the new and
630 ELM2/CLM5 defaults. Moreover, the new parameters indicate larger slopes in mountainous
631 regions and more distinct elevation differences in areas such as Greenland and the Tibetan Plateau
632 compared to ELM2/CLM5. These differences potentially highlight enhanced accuracy and
633 sophistication of the new 1k parameters. Their enhanced resolution and rigorous validation suggest
634 a substantial capacity to improve ESMs modeling. Additionally, the richness of multi-year data
635 for LULC, LAI, and SAI in these datasets is especially valuable for examining land use and cover
636 changes, urbanization trends, deforestation impacts, and agricultural transformations.

637
638 The new 1 km land surface parameters can improve k-scale offline LSMs modeling by better
639 capturing spatial surface heterogeneity. As evidenced by the 1 km ELM simulation over CONUS,

640 soil properties, vegetation properties, and topographic factors contribute a lot to the spatial
641 heterogeneities of ELM water and energy simulations. Upscaling 1 km to a coarser 12 km
642 resolution, we observe significant spatial information loss, with SM experiencing an average loss
643 of 31%, and LH, ELR, and ASR experiencing around 50% information loss on average (Figure
644 12). This conclusion is in line with the results of Vergopolan et al. (2022), which showed a
645 substantial loss of spatial information in soil moisture when upscaling from 30 m to 1 km resolution,
646 with an average loss of approximately 48% and up to 80% over the CONUS region. The XML
647 analysis reveals that the spatial variability and information loss of ELM2 simulations are
648 influenced by the spatial variability and information loss of the different variables of land surface
649 parameters, as well as the mean precipitation and temperature (Figures 11 and 12). Our findings
650 highlight the critical role of land surface parameters in contributing to the spatial variability of
651 water and energy in land surface simulations, showcasing the value of the developed high-
652 resolution datasets. Another implementation example where our 1 km land surface parameters can
653 be beneficial is in hillslope-scale simulations, which are fundamental for organizing water, energy,
654 and biogeochemical processes (Fan et al., 2019). Krakauer et al. (2014) have highlighted the
655 significance of between-cell groundwater flow, which becomes comparable in magnitude to
656 recharge at grid spacings smaller than 10 km. Advancements have been made in ESMs to address
657 hillslope-scale processes, including the representation of intra-hillslope lateral subsurface flow
658 within grid cells in CLM5 (Swenson et al., 2019), the development of explicit lateral flow
659 processes between grid cells (Qiu et al., 2023), and the incorporation of topographic radiation
660 effects within and between grid cells (Hao et al., 2021). Another notable example is the integrated
661 hydrology-land surface model ParFlow-CLM, which incorporates three-dimensional groundwater
662 flow, two-dimensional overland flow, and land surface exchange processes (Maxwell, 2013).

663 ParFlow-CLM has demonstrated remarkable reliability in reproducing hydrologic processes, such
664 as its simulations at 3 km resolution for pan-European and 1 km resolution for CONUS (Naz et al.,
665 2023; O'Neill et al., 2021). More recently, Fang et al. (2022) coupled ParFlow with ELM and the
666 Functionally Assembled Terrestrial Ecosystem Simulator (FATES) to simulate carbon-hydrology
667 interactions at hillslope scale. By incorporating our 1 km datasets and leveraging these
668 advancements, we can improve simulations of hillslope-scale processes and enhance our
669 understanding of water and energy dynamics within ESMs.

670
671 Additionally, the new land surface parameters are also a timely resource for supporting the
672 emerging need for k-scale Earth system modeling, particularly in improving land-atmosphere
673 interaction processes. Representing the impact of spatial heterogeneity on land-atmosphere
674 interaction processes is a major challenge in Earth system modeling. Taking E3SM as an example,
675 researchers have proposed three key approaches to enhance spatial heterogeneity representation to
676 address this challenge. In line with these approaches, our newly developed 1 km land surface
677 parameters offer promising opportunities for improving land-atmosphere coupling within ESMs.
678 The first approach to enhance the representation of spatial heterogeneity is to directly conduct
679 simulations at high resolution. For instance, the Simple Cloud-Resolving E3SM Atmosphere
680 Model (SCREAM) has been used to perform global simulations at 3.25 km (Caldwell et al., 2021),
681 although the land surface parameters were based on coarser resolution datasets. By utilizing the
682 new 1 km land surface parameters, we can enhance the representation of land surface heterogeneity
683 within the ELM component of SCREAM, potentially improving modeling of land-atmosphere
684 coupling. The second and third approaches focus on improving the representation of land surface
685 heterogeneity within ESMs run at a coarse resolution while accounting for subgrid heterogeneity

686 in two different ways. In the second approach, the Cloud Layers Unified By Binormals (CLUBB)
687 has been implemented in E3SM Atmosphere Model (EAM) version 1 (Rasch et al., 2019;
688 Bogenschutz et al., 2013), to better account for subgrid atmospheric heterogeneity of turbulent
689 mixing, shallow convection, and cloud macrophysics. Recently, Huang et al. (2022) developed a
690 novel land-atmosphere coupling scheme in EAM that enables the communication of subgrid land
691 surface heterogeneity information to the atmosphere model with CLUBB, significantly impacting
692 boundary layer dynamics. The new 1km datasets can provide more accurate land surface
693 representations of the variability of individual patches and the inter-patch variability that were
694 used in Huang et al. (2022). The third approach is the Multiple Atmosphere Multiple Land (MAML)
695 approach used in the multiscale modeling framework (MMF) in which a cloud resolving model
696 (CRM) is embedded within each grid cell of the atmosphere (Baker et al., 2019; Lin et al., 2023;
697 Lee et al., 2023). In the MAML approach, each CRM column within the atmosphere grid is coupled
698 directly with its own independent land surface. This enables a more explicit representation of the
699 impact of spatial heterogeneity on land-atmosphere interactions within each grid and has shown
700 notable impacts on water and energy simulations (Baker et al., 2019; Lin et al., 2023). Lee et al.
701 (2023) highlighted the limitation of the current MAML approach, which utilizes the same land
702 surface characteristics for each land surface model interacting with the CRM column within the
703 same grid, which could lead to a weak representation of land-atmosphere interactions. To address
704 this limitation, incorporating the new 1 km land surface parameters within the MAML approach
705 can provide more detailed information about land surface heterogeneity, enabling a more accurate
706 capture of land-atmosphere interactions.

707

708 Evaluation of k-scale simulations, while essential, faces significant challenges as merely updating
709 the land surface input data to the new 1k parameters for k-scale simulations [does not](#) guarantee
710 improved model performance. [This is clearly evidenced in our ELM demonstration simulations,](#)
711 [where, despite relatively low CONUS averaged biases for water and energy simulations, the spatial](#)
712 [variation in these biases cannot be overlooked, with some regions exhibiting notably larger biases.](#)
713 [It is important to emphasize that enhancing model performance requires not just updated input](#)
714 [data, but also appropriate calibration of model parameters and faithful model structures to](#)
715 [represent various processes.](#) First, LSMs and ESMs that have been adapted for simulations at
716 coarser resolutions commensurate with the resolutions of previous land surface data require
717 recalibration for effective high-resolution modeling. This necessity for recalibration is echoed by
718 Ruiz-Vásquez et al., (2023), who noted that updating the ECMWF system with new land surface
719 data did not inherently improve performance, but improvements were seen after recalibrating key
720 soil and vegetation-related parameters. Second, high-resolution modeling requires the
721 incorporation of new physical processes crucial at finer scales. For example, hillslope-scale
722 processes like lateral flow and topography-radiation interactions are key to water and energy fluxes
723 at high resolution (Han et al., 2023; Hao et al., 2021). With increased heterogeneity at higher
724 resolutions, larger differences in land surface properties such as vegetation water use strategies
725 requires more attention to plant hydraulics besides the traditional focus on soil hydraulics for a
726 more accurate depiction of plant water use, as highlighted by Li et al., (2021). Third, the lack of
727 high-resolution benchmarks for large-scale applications, like k-scale atmospheric forcing data,
728 remains a challenge, despite the availability of relative coarse resolution global datasets such as
729 ERA5_Land (Muñoz-Sabater et al., 2021) and MSWX (Beck et al., 2021). Additionally, using soil
730 moisture as an example, multiple high-resolution datasets exhibit significantly different

731 performance when compared to in-situ measurements (Beck et al., 2021). Lastly, when evaluating
732 simulations against benchmarks, it is crucial not only to assess absolute differences using metrics
733 like bias and root mean square error but also to examine other metrics, such as the relationships
734 between physical variables (e.g., rainfall vs. runoff; soil moisture vs. evapotranspiration),
735 information loss, and the tail quantiles of the probability distribution functions for simulations (e.g.,
736 extreme events, [Li et al., 2020](#)).

737
738 There are certain opportunities for future development of 1k parameters. The urban extension may
739 vary based on data sources, urban definitions, and the algorithms employed, such as those derived
740 from harmonized nighttime lights (Zhao et al., 2022), global artificial impervious area (GAIA, Li
741 et al., 2020b; Gong et al., 2020), urban expansion (Liu et al., 2020; Kuang et al., 2021),
742 necessitating careful consideration in specific modeling applications. Additionally, urban
743 classification in J2010, based on global building height data, is limited by the lack of a consistent
744 and publicly accessible global dataset, despite available regional data for Europe (Frantz et al.,
745 2021), the US (Li et al., 2020a), and China (Cao and Huang, 2021; Yang and Zhao, 2022), thus
746 posing challenges to future urban classification enhancements. Incorporating local climate zones
747 offers a promising approach for urban classification and modeling. Moreover, the multiple-year
748 high-resolution PFT maps like the ones developed by the European Space Agency's Climate
749 Change Initiative could be used to further extend this dataset for a longer period (Harper et al.,
750 2023). Soil color, crucial for soil albedo and surface energy balance, lacks extensive global datasets
751 for ESMs modeling, but the global soil color map derived by Rizzo et al. (2023) offers potential
752 for further kilometer-scale ESMs and LSMs modeling.

753

754 The strategic aggregation of high-resolution parameters to coarser resolutions are crucial to
755 maintain accuracy and effectiveness in modeling applications. For instance, in soil properties, the
756 basic parameters (e.g., percent sand) are often utilized to derive secondary parameters (e.g.,
757 saturated water content). This aggregation procedure, whether performs before or after deriving
758 secondary parameters—known as 'aggregating first' and 'aggregating after'—is influenced by the
759 non-linear relationships between basic and derived parameters, with the latter method generally
760 preferred (Shangguan et al., 2014; Dai et al., 2019). Our study's initial approach in upscaling soil-
761 and topography-related parameters follows the 'aggregate first' approach, aligning with the
762 structure of models like ELM2 and CLM5. Conversely, models such as Common Land Model
763 (CoLM, Dai et al., 2003) and community Noah with multi-parameterization options (Noah-MP,
764 He et al., 2023; Niu et al., 2011; Yang et al., 2011) integrate secondary derived soil related
765 parameters directly as inputs, effectively demonstrating the advantages of the 'aggregating after'
766 approach. By leveraging secondary derived parameters from comprehensive databases such as
767 SoilGrids (Hengl et al., 2017) and GSDE (Shangguan et al., 2014), these models provide a valuable
768 framework for future development of models like ELM2 and CLM5 by directly integrating
769 secondary derived parameters.
770

771 **6. Data availability**

772 The 1 km land surface parameters are publicly available at [Zenodo](https://zenodo.org/records/10523833):
773 <https://zenodo.org/records/10523833> (Li et al., 2024) and PNNL Datahub:
774 <https://doi.org/10.25584/PNNLDH/1986308> (Li et al., 2023).
775

Deleted: 5

776 **7. Conclusions**

777 We developed 1 km global land surface parameters using the latest available datasets covering
778 multiple years from 2001 to 2020. These parameters comprise four categories: LULC of PFTs and
779 non-vegetative land cover, vegetation properties, soil properties, and topographic factors. The new
780 1k parameters, when compared to the K2012 and ELM2/CLM5 default datasets, display
781 significant differences, indicating their potential superiority stemming from the utilization of latest
782 and more advanced data sources. The 1 km resolution ELM simulations conducted over CONUS
783 demonstrate the valuable capabilities of the new datasets in enabling k-scale land surface modeling.
784 Through scaling analysis of the 1 km resolution simulations within $0.5^\circ \times 0.5^\circ$ boxes where spatial
785 heterogeneity of the simulations is induced only by spatial heterogeneity of the land surface
786 parameters, we revealed the significant impact of land surface parameters on the spatial variability
787 of water and energy simulations. The spatial information loss of these simulations over CONUS
788 is significant when upscaling from 1 km to a coarser 12 km resolution, with an average ranging
789 from 31% to 54% and up to more than 90%. The XML analysis reveals that the spatial variability
790 and spatial information loss of ELM2 simulations are primarily impacted by the spatial variability
791 and information loss of soil properties, vegetation properties and topography factors, as well as the
792 mean climate conditions of precipitation and temperature. Furthermore, the spatial variability of
793 water and energy in the 1 km simulations is not dominated by the spatial heterogeneity of any land

Deleted: 6

796 surface parameters, suggesting the usefulness of the multi-parameter high-resolution land surface
797 parameter dataset. [Furthermore, the comparison against four benchmark datasets indicates that](#)
798 [ELM generally performs well in simulating soil moisture and surface energy fluxes.](#) The
799 availability of 1 km land surface parameters is a valuable resource that addresses the emerging
800 needs of k-scale LSMs and ESMS modeling. By providing accurate and precise information, these
801 1 km land surface parameters will significantly enhance our understanding of the water, carbon,
802 and energy cycles under global change.

803

804 **Author contributions**

805 LL, GB, and DH designed the study, processed the datasets, conducted experiments, and drafted
806 the manuscript. LRL contributed to the conceptual design, discussion of results, and manuscript
807 revisions.

808

809 **Acknowledgments**

810 This study is supported by the US Department of Energy (DOE) Office of Science Biological and
811 Environmental Research as part of the Regional and Global Model Analysis (RGMA) program
812 area through the collaborative, multi-program Integrated Coastal Modeling (ICoM) project. This
813 study used DOE's Biological and Environmental Research Earth System Modeling program's
814 Compy computing cluster at Pacific Northwest National Laboratory. Pacific Northwest National
815 Laboratory is operated for the US Department of Energy by Battelle Memorial Institute under
816 contract DE-AC05-76RL01830. DH acknowledges the support from the US DOE, Office of
817 Science, Office of Biological and Environmental Research, Earth System Model Development
818 program area, as part of the Climate Process Team projects. Our thanks to Ye Liu and Teklu Tesfa
819 at PNNL for guidance on the canopy height dataset and K2012 datasets, respectively. We deeply
820 appreciate the reviewers for their valuable insights and suggestions.

821

822 **Financial support**

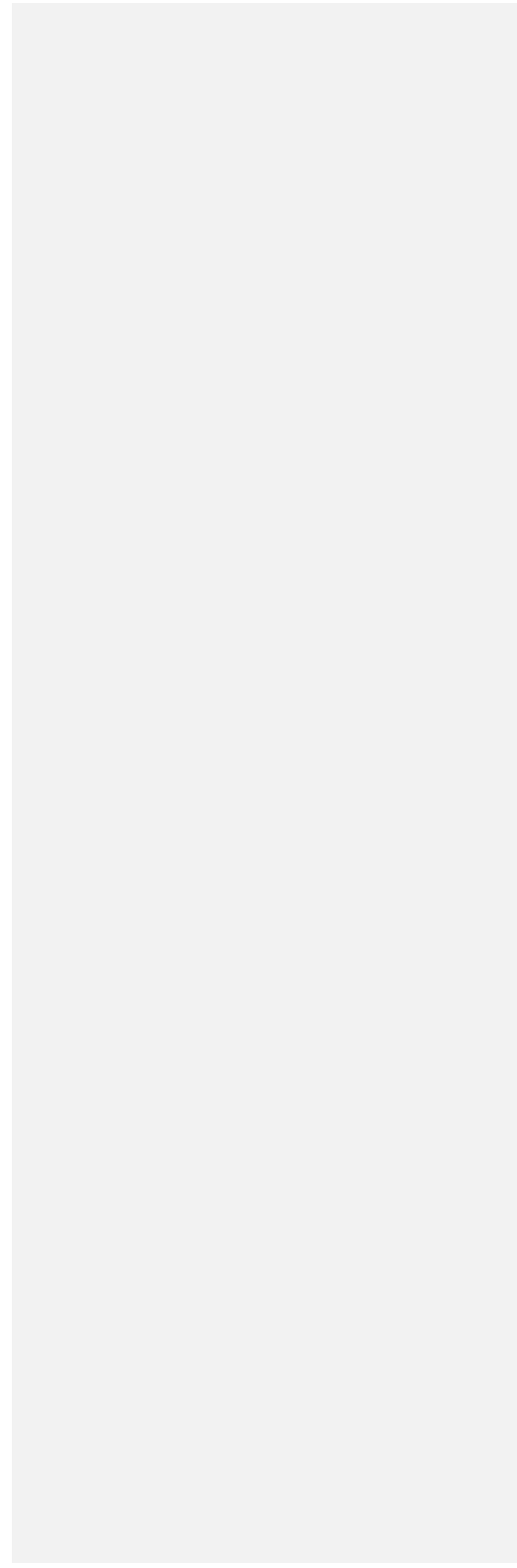
823 This work was supported by the Regional and Global Modeling and Analysis program area of the US
824 Department of Energy, Office of Science, Office of Biological and Environmental Research, as
825 part of the multi-program, collaborative integrated Coastal Modeling (ICoM) project (grant no.
826 KP1703110/75415).

827

828 **Competing interests**

829 At least one of the (co-)authors is a member of the editorial board of the Earth System Science

830 Data. The authors have no other competing interests to declare.



831 **Reference**

- 832 Arendt, A., Bliss, A., Bolch, T., et al.: Randolph Glacier Inventory—A Dataset of Global Glacier
833 Outlines Version: 1.0, Global Land Ice Measurements from Space, Boulder Colorado, USA.
834 Digital Media, 2012.
- 835 Baker, I. T., Denning, A. S., Dazlich, D. A., Harper, A. B., Branson, M. D., Randall, D. A.,
836 Phillips, M. C., Haynes, K. D., and Gallup, S. M.: Surface-Atmosphere Coupling Scale, the Fate
837 of Water, and Ecophysiological Function in a Brazilian Forest, *J Adv Model Earth Sy*, 11, 2523–
838 2546, <https://doi.org/10.1029/2019ms001650>, 2019.
- 839 Batjes, N.H.: ISRIC-WISE derived soil properties on a 5 by 5 arc-minutes global grid. Report
840 2006/02, available through : <http://www.isric.org>, 2006.
- 841 Beck, H. E., Van Dijk, A. I., Larraondo, P. R., McVicar, T. R., Pan, M., Dutra, E., & Miralles, D.
842 G.: MSWX: Global 3-hourly 0.1 bias-corrected meteorological data including near-real-time
843 updates and forecast ensembles, *BAMS*, 103(3), E710-E732, [https://doi.org/10.1175/BAMS-D-](https://doi.org/10.1175/BAMS-D-21-0145.1)
844 [21-0145.1](https://doi.org/10.1175/BAMS-D-21-0145.1), 2022.
- 845 Beck, H. E., Pan, M., Miralles, D. G., Reichle, R. H., Dorigo, W. A., Hahn, S., Sheffield, J.,
846 Karthikeyan, L., Balsamo, G., Parinussa, R. M., van Dijk, A. I. J. M., Du, J., Kimball, J. S.,
847 Vergopolan, N., and Wood, E. F.: Evaluation of 18 satellite- and model-based soil moisture
848 products using in situ measurements from 826 sensors, *Hydrol Earth Syst Sci*, 25, 17–40,
849 <https://doi.org/10.5194/hess-25-17-2021>, 2021.
- 850 Bogenschutz, P. A., Gettelman, A., Morrison, H., Larson, V. E., Craig, C., and Schanen, D. P.:
851 Higher-Order Turbulence Closure and Its Impact on Climate Simulations in the Community
852 Atmosphere Model, *J Climate*, 26, 9655–9676, <https://doi.org/10.1175/jcli-d-13-00075.1>, 2013.
- 853 Bonan, G. B., Oleson, K. W., Vertenstein, M., Levis, S., Zeng, X., Dai, Y., Dickinson, R. E., and
854 Yang, Z.-L.: The Land Surface Climatology of the Community Land Model Coupled to the
855 NCAR Community Climate Model*, *J Climate*, 15, 3123–3149, [https://doi.org/10.1175/1520-](https://doi.org/10.1175/1520-0442(2002)015<3123:tlscot>2.0.co;2)
856 [0442\(2002\)015<3123:tlscot>2.0.co;2](https://doi.org/10.1175/1520-0442(2002)015<3123:tlscot>2.0.co;2), 2002.
- 857 Bonan, G. B., Levis, S., Kergoat, L., & Oleson, K. W.: Landscapes as patches of plant functional
858 types: An integrating concept for climate and ecosystem models. *Global Biogeochemical Cycles*,
859 16(2), 5-1–5-23. <https://doi.org/10.1029/2000gb001360>, 2002
- 860 Bou-Zeid, E., Anderson, W., Katul, G. G., and Mahrt, L.: The Persistent Challenge of Surface
861 Heterogeneity in Boundary-Layer Meteorology: A Review, *Bound-lay Meteorol*, 177, 227–245,
862 <https://doi.org/10.1007/s10546-020-00551-8>, 2020.
- 863 Caldwell, P. M., Mametjanov, A., Tang, Q., Roedel, L. P. V., Golaz, J., Lin, W., Bader, D. C.,
864 Keen, N. D., Feng, Y., Jacob, R., Maltrud, M. E., Roberts, A. F., et al.: The DOE E3SM Coupled
865 Model Version 1: Description and Results at High Resolution, *J Adv Model Earth Sy*, 11, 4095–
866 4146, <https://doi.org/10.1029/2019ms001870>, 2019.

867 Caldwell, P. M., Terai, C. R., Hillman, B., Keen, N. D., Bogenschutz, P., Lin, W., et al.:
868 Convection-Permitting Simulations With the E3SM Global Atmosphere Model, *J Adv Model*
869 *Earth Sy*, 13, <https://doi.org/10.1029/2021ms002544>, 2021.

870 Cao, Y. and Huang, X.: A deep learning method for building height estimation using high-
871 resolution multi-view imagery over urban areas: A case study of 42 Chinese cities, *Remote Sens*
872 *Environ*, 264, 112590, <https://doi.org/10.1016/j.rse.2021.112590>, 2021.

873 Chaney, N. W., Huijgevoort, M. H. J. V., Shevliakova, E., Malyshev, S., Milly, P. C. D.,
874 Gauthier, P. P. G., and Sulman, B. N.: Harnessing big data to rethink land heterogeneity in Earth
875 system models, *Hydrol Earth Syst Sc*, 22, 3311–3330, [https://doi.org/10.5194/hess-22-3311-](https://doi.org/10.5194/hess-22-3311-2018)
876 [2018](https://doi.org/10.5194/hess-22-3311-2018), 2018.

877 Change, N. C.: Think big and model small, *Nat Clim Change*, 12, 493–493,
878 <https://doi.org/10.1038/s41558-022-01399-1>, 2022.

879 Chen, T. and Guestrin, C.: XGBoost: A Scalable Tree Boosting System, *Proc 22nd Acm Sigkdd*
880 *Int Conf Knowl Discov Data Min*, 785–794, <https://doi.org/10.1145/2939672.2939785>, 2016.

881 Dai, Y., Zeng, X., Dickinson, R. E., Baker, I., Bonan, G. B., Bosilovich, M. G., et al.: The
882 common land model, *BAMS*, 84(8), 1013–1024, <https://doi.org/10.1175/BAMS-84-8-1013>,
883 2003.

884 Dai, Y., Shangguan, W., Wei, N., Xin, Q., Yuan, H., Zhang, S., Liu, S., Lu, X., Wang, D., and
885 Yan, F.: A Review of the Global Soil Property Maps for Earth System Models, *SOIL*, 5, 137–
886 158. <https://doi.org/10.5194/soil-5-137-2019>, 2019.

887 Defries, R. S., Hansen, M. C., Townshend, J. R. G., Janetos, A. C., and Loveland, T. R.: A new
888 global 1-km dataset of percentage tree cover derived from remote sensing: GLOBAL
889 PERCENTAGE TREE COVER FROM REMOTE SENSING, *Global Change Biol*, 6, 247–254,
890 <https://doi.org/10.1046/j.1365-2486.2000.00296.x>, 2000.

891 Dozier, J.: Revisiting Topographic Horizons in the Era of Big Data and Parallel Computing, *Ieee*
892 *Geosci Remote S*, 19, 1–5, <https://doi.org/10.1109/lgrs.2021.3125278>, 2022.

893 Fan, Y., Clark, M., Lawrence, D. M., Swenson, S., Band, L. E., Brantley, S. L., et al.: Hillslope
894 Hydrology in Global Change Research and Earth System Modeling, *Water Resour Res*, 55,
895 1737–1772, <https://doi.org/10.1029/2018wr023903>, 2019.

896 Frantz, D., Schug, F., Okujeni, A., Navacchi, C., Wagner, W., Linden, S. van der, and Hostert,
897 P.: National-scale mapping of building height using Sentinel-1 and Sentinel-2 time series,
898 *Remote Sens Environ*, 252, 112128, <https://doi.org/10.1016/j.rse.2020.112128>, 2021.

899 Friedl, M. A., McIver, D. K., Hodges, J. C. F., Zhang, X. Y., Muchoney, D., Strahler, A. H.,
900 Woodcock, C. E., Gopal, S., Schneider, A., Cooper, A., Baccini, A., Gao, F., and Schaaf, C.:

901 Global land cover mapping from MODIS: algorithms and early results, *Remote Sens Environ*,
902 83, 287–302, [https://doi.org/10.1016/s0034-4257\(02\)00078-0](https://doi.org/10.1016/s0034-4257(02)00078-0), 2002.

903 Friedl, M. A., Sulla-Menashe, D., Tan, B., Schneider, A., Ramankutty, N., Sibley, A., and
904 Huang, X.: MODIS Collection 5 global land cover: Algorithm refinements and characterization
905 of new datasets, *Remote Sens Environ*, 114, 168–182, <https://doi.org/10.1016/j.rse.2009.08.016>,
906 2010.

907 Friedl, M., Sulla-Menashe, D.: MCD12Q1 MODIS/Terra+Aqua Land Cover Type Yearly L3
908 Global 500m SIN Grid V006 [Data set]. NASA EOSDIS Land Processes DAAC. Accessed
909 2022-11-21 from <https://doi.org/10.5067/MODIS/MCD12Q1.006>, 2019.

910 Giorgi, F. and Avissar, R.: Representation of heterogeneity effects in Earth system modeling:
911 Experience from land surface modeling, *Rev Geophys*, 35, 413–437,
912 <https://doi.org/10.1029/97rg01754>, 1997.

913 Gorelick, N., Hancher, M., Dixon, M., Ilyushchenko, S., Thau, D., & Moore, R.: Google Earth
914 Engine: Planetary-scale geospatial analysis for everyone. *Remote Sensing of Environment*, 202,
915 18–27. <https://doi.org/10.1016/j.rse.2017.06.031>, 2017.

916 Gong, P., Li, X., Wang, J., Bai, Y., Chen, B., Hu, T., Liu, X., Xu, B., Yang, J., Zhang, W., and
917 Zhou, Y.: Annual maps of global artificial impervious area (GAIA) between 1985 and 2018,
918 *Remote Sens Environ*, 236, 111510, <https://doi.org/10.1016/j.rse.2019.111510>, 2020.

919 Gorelick, N., Hancher, M., Dixon, M., Ilyushchenko, S., Thau, D., and Moore, R.: Google Earth
920 Engine: Planetary-scale geospatial analysis for everyone, *Remote Sens Environ*, 202, 18–27,
921 <https://doi.org/10.1016/j.rse.2017.06.031>, 2017.

922 Hansen, M. C., DeFries, R. S., Townshend, J. R. G., Carroll, M., Dimiceli, C., and Sohlberg, R.
923 A.: Global Percent Tree Cover at a Spatial Resolution of 500 Meters: First Results of the MODIS
924 Vegetation Continuous Fields Algorithm, *Earth Interact*, 7, 1–15, [https://doi.org/10.1175/1087-
925 3562\(2003\)007<0001:gptcaa>2.0.co;2](https://doi.org/10.1175/1087-3562(2003)007<0001:gptcaa>2.0.co;2), 2003.

926 Hao, D., Bisht, G., Huang, M., Ma, P., Tesfa, T., Lee, W., Gu, Y., and Leung, L. R.: Impacts of
927 Sub-Grid Topographic Representations on Surface Energy Balance and Boundary Conditions in
928 the E3SM Land Model: A Case Study in Sierra Nevada, *J Adv Model Earth Sy*, 14,
929 <https://doi.org/10.1029/2021ms002862>, 2022.

930 Harper, K. L., Lamarche, C., Hartley, A., Peylin, P., Ottlé, C., Bastrikov, V., Martín, R. S.,
931 Bohnenstengel, S. I., Kirches, G., Boettcher, M., Shevchuk, R., Brockmann, C., and Defourny,
932 P.: A 29-year time series of annual 300 m resolution plant-functional-type maps for climate
933 models, *Earth Syst Sci Data*, 15, 1465–1499, <https://doi.org/10.5194/essd-15-1465-2023>, 2023.

934 Hengl, T., Jesus, J. M. de, Heuvelink, G. B. M., Gonzalez, M. R., Kilibarda, M., Blagotić, A.,
935 Shangguan, W., Wright, M. N., et al.: SoilGrids250m: Global gridded soil information based on
936 machine learning, *Plos One*, 12, e0169748, <https://doi.org/10.1371/journal.pone.0169748>, 2017.

- 937 Hewitt, H., Fox-Kemper, B., Pearson, B., Roberts, M., and Klocke, D.: The small scales of the
938 ocean may hold the key to surprises, *Nat Clim Change*, 12, 496–499,
939 <https://doi.org/10.1038/s41558-022-01386-6>, 2022.
- 940 He, C., Valayamkunnath, P., Barlage, M., Chen, F., Gochis, D., Cabell, R., Schneider, T.,
941 Rasmussen, R., Niu, G.-Y., Yang, Z.-L., Niyogi, D., and Ek, M.: Modernizing the open-source
942 community Noah with multi-parameterization options (Noah-MP) land surface model (version
943 5.0) with enhanced modularity, interoperability, and applicability, *Geosci Model Dev*, 16, 5131–
944 5151, <https://doi.org/10.5194/gmd-16-5131-2023>, 2023.
- 945 Hijmans, R. J., Cameron, S. E., Parra, J. L., Jones, P. G., and Jarvis, A.: Very high resolution
946 interpolated climate surfaces for global land areas, *International Journal of Climatology*, 25,
947 1965–1978, <https://doi.org/10.1002/joc.1276>, 2005.
- 948 Hu, Z., Islam, S., and Cheng, Y.: Statistical characterization of remotely sensed soil moisture
949 images, *Remote Sens Environ*, 61, 310–318, [https://doi.org/10.1016/s0034-4257\(97\)89498-9](https://doi.org/10.1016/s0034-4257(97)89498-9),
950 1997.
- 951 Huang, M., Ma, P.-L., Chaney, N. W., Hao, D., Bisht, G., Fowler, M. D., Larson, V. E., and
952 Leung, L. R.: Representing surface heterogeneity in land-atmosphere coupling in E3SMv1
953 single-column model over ARM SGP during summertime, *Geoscientific Model Dev Discuss*,
954 2022, 1–20, <https://doi.org/10.5194/gmd-2021-421>, 2022.
- 955 Huang, F., Jiang, S., Zhan, W., Bechtel, B., Liu, Z., Demuzere, M.: Mapping local climate zones
956 for cities: A large review, *Remote Sens. Environ.*, 292, 113573,
957 <https://doi.org/10.1016/j.rse.2023.113573>, 2023.
- 958 Hugelius, G., Tarnocai, C., Broll, G., Canadell, J. G., Kuhry, P., and Swanson, D. K.: The
959 Northern Circumpolar Soil Carbon Database: spatially distributed datasets of soil coverage and
960 soil carbon storage in the northern permafrost regions, *Earth Syst. Sci. Data*, 5, 3–13,
961 <https://doi.org/10.5194/essd-5-3-2013>, 2013.
- 962 IGBP: Global Soil Data Task (IGBP-DIS, ISO-image of CD). International Geosphere-Biosphere
963 Program, PANGAEA, <https://doi.org/10.1594/PANGAEA.869912>, 2000.
- 964 Jackson, T. L., Feddema, J. J., Oleson, K. W., Bonan, G. B., and Bauer, J. T.: Parameterization
965 of Urban Characteristics for Global Climate Modeling, *Ann Assoc Am Geogr*, 100, 848–865,
966 <https://doi.org/10.1080/00045608.2010.497328>, 2010.
- 967 Jarvis, A., H.I. Reuter, A. Nelson, E. Guevara.: Hole-filled SRTM for the globe Version 4,
968 available from the CGIAR-CSI SRTM 90m Database: <https://srtm.csi.cgiar.org>, 2008.
- 969 Ji, P. and Yuan, X.: High-Resolution Land Surface Modeling of Hydrological Changes Over the
970 Sanjiangyuan Region in the Eastern Tibetan Plateau: 2. Impact of Climate and Land Cover
971 Change, *J Adv Model Earth Sy*, 10, 2829–2843, <https://doi.org/10.1029/2018ms001413>, 2018.

972 Ji, P., Yuan, X., Shi, C., Jiang, L., Wang, G., and Yang, K.: A Long-Term Simulation of Land
973 Surface Conditions at High Resolution over Continental China, *J Hydrometeorol*, 24, 285–314,
974 <https://doi.org/10.1175/jhm-d-22-0135.1>, 2023.

975 Ke, Y., Leung, L. R., Huang, M., Coleman, A. M., Li, H., and Wigmosta, M. S.: Development of
976 high resolution land surface parameters for the Community Land Model, *Geosci Model Dev*, 5,
977 1341–1362, <https://doi.org/10.5194/gmd-5-1341-2012>, 2012.

978 Ke, Y., Leung, L. R., Huang, M., and Li, H.: Enhancing the representation of subgrid land
979 surface characteristics in land surface models, *Geosci Model Dev*, 6, 1609–1622,
980 <https://doi.org/10.5194/gmd-6-1609-2013>, 2013.

981 Kim, H.: Global Soil Wetness Project Phase 3 Atmospheric Boundary Conditions (Experiment 1)
982 [Data set]. Data Integration and Analysis System (DIAS). <https://doi.org/10.20783/DIAS.501>,
983 2017.

984 Kourzeneva, E.: Global dataset for the parameterization of lakes in Numerical Weather
985 Prediction and Climate modeling. ALADIN Newsletter, No 37, July-December, 2009, F.
986 Bouttier and C. Fischer, Eds., Meteo-France, Toulouse, France, 46-53, 2009.

987 Kourzeneva, E.: External data for lake parameterization in Numerical Weather Prediction and
988 climate modeling. *Boreal Environment Research*, 15, 165-177, 2010.

989 Krakauer, N. Y., Li, H., and Fan, Y.: Groundwater flow across spatial scales: importance for
990 climate modeling, *Environ Res Lett*, 9, 034003, <https://doi.org/10.1088/1748-9326/9/3/034003>,
991 2014.

992 Kuang, W., Du, G., Lu, D., Dou, Y., Li, X., Zhang, S., Chi, W., Dong, J., Chen, G., Yin, Z., Pan,
993 T., Hamdi, R., Hou, Y., Chen, C., Li, H., and Miao, C.: Global observation of urban expansion
994 and land-cover dynamics using satellite big-data, *Sci Bull*, 66, 297–300,
995 <https://doi.org/10.1016/j.scib.2020.10.022>, 2021.

996 Lang, N., Jetz, W., Schindler, K., and Wegner, J. D.: A high-resolution canopy height model of
997 the Earth. *Nat Ecol Evol*, <https://doi.org/10.1038/s41559-023-02206-6>, 2023.

998 Lawrence, D. M., Fisher, R. A., Koven, C. D., Oleson, K. W., Swenson, S. C., Bonan, G., et al.:
999 The Community Land Model Version 5: Description of New Features, Benchmarking, and
1000 Impact of Forcing Uncertainty, *J Adv Model Earth Sy*, 11, 4245–4287,
1001 <https://doi.org/10.1029/2018ms001583>, 2019.

1002 Lawrence, D., Fisher, R., Koven, C., Oleson, K., Swenson, S., et al. (2018). Technical
1003 description of version 5.0 of the Community Land Model (CLM). National Center for
1004 Atmospheric Research, University Corporation for Atmospheric Research, Boulder, CO.
1005 https://escomp.github.io/ctsm-docs/versions/release-clm5.0/html/tech_note/index.html

1006 Lee, J., Hannah, W. M., and Bader, D. C.: Representation of atmosphere induced heterogeneity
1007 in land – atmosphere interactions in E3SM-MMFv2, *Geoscientific Model Dev Discuss*, 2023, 1–
1008 21, <https://doi.org/10.5194/gmd-2023-55>, 2023.

1009 Leng, G., Huang, M., Tang, Q., Sacks, W. J., Lei, H., and Leung, L. R.: Modeling the effects of
1010 irrigation on land surface fluxes and states over the conterminous United States: Sensitivity to
1011 input data and model parameters, *J Geophys Res Atmospheres*, 118, 9789–9803,
1012 <https://doi.org/10.1002/jgrd.50792>, 2013.

1013 Leung, L. R., Bader, D. C., Taylor, M. A., and McCoy, R. B.: An Introduction to the E3SM
1014 Special Collection: Goals, Science Drivers, Development, and Analysis, *J Adv Model Earth Sy*,
1015 12, <https://doi.org/10.1029/2019ms001821>, 2020.

1016 Li, L., Yang, Z., Matheny, A. M., Zheng, H., Swenson, S. C., Lawrence, D. M., Barlage, M.,
1017 Yan, B., McDowell, N. G., and Leung, L. R.: Representation of Plant Hydraulics in the Noah-
1018 MP Land Surface Model: Model Development and Multiscale Evaluation, *J Adv Model Earth*
1019 *Sy*, 13, <https://doi.org/10.1029/2020ms002214>, 2021.

1020 Li, L., Bisht, G., and Leung, L. R.: Spatial heterogeneity effects on land surface modeling of
1021 water and energy partitioning, *Geosci Model Dev*, 15, 5489–5510, <https://doi.org/10.5194/gmd-15-5489-2022>, 2022.

1023 Li, X., Zhou, Y., Gong, P., Seto, K. C., and Clinton, N.: Developing a method to estimate
1024 building height from Sentinel-1 data, *Remote Sens Environ*, 240, 111705,
1025 <https://doi.org/10.1016/j.rse.2020.111705>, 2020a.

1026 Li, X., Gong, P., Zhou, Y., Wang, J., Bai, Y., Chen, B., Hu, T., Xiao, Y., et al.: Mapping global
1027 urban boundaries from the global artificial impervious area (GAIA) data, *Environ Res Lett*, 15,
1028 094044, <https://doi.org/10.1088/1748-9326/ab9be3>, 2020b.

1029 [Li, L., She, D., Zheng, H., Lin, P., and Yang, Z.-L.: Elucidating Diverse Drought Characteristics](https://doi.org/10.1175/JHM-D-19-0290.1)
1030 [from Two Meteorological Drought Indices \(SPI and SPEI\) in China, *J Hydrometeorol*, 21,](https://doi.org/10.1175/JHM-D-19-0290.1)
1031 <https://doi.org/10.1175/JHM-D-19-0290.1>, 2020.

1032 Li, L., Bisht, G., Hao, D., Leung, L.R.: Global 1km Land Surface Parameters for Kilometer
1033 Scale Earth System Modeling, Pacific Northwest National Laboratory DataHub [data set],
1034 <https://doi.org/10.25584/PNNLDH/1986308>, 2023.

1035 [Li, L., Bisht, G., Hao, D., Leung, L.R.: Global 1km Land Surface Parameters for Kilometer-](https://doi.org/10.5281/zenodo.10523833)
1036 [Scale Earth System Modeling \[Data set\]. Zenodo. https://doi.org/10.5281/zenodo.10523833,](https://doi.org/10.5281/zenodo.10523833)
1037 [2024](https://doi.org/10.5281/zenodo.10523833)

1038 Lin, G., Leung, L. R., Lee, J., Harrop, B. E., Baker, I. T., Branson, M. D., Denning, A. S., Jones,
1039 C. R., Ovchinnikov, M., Randall, D. A., and Yang, Z.: Modeling Land-Atmosphere Coupling at
1040 Cloud-Resolving Scale Within the Multiple Atmosphere Multiple Land (MAML) Framework in
1041 SP-E3SM, *J Adv Model Earth Sy*, 15, <https://doi.org/10.1029/2022ms003101>, 2023.

- 1042 Liu, S., Shao, Y., Kunoth, A., and Simmer, C.: Impact of surface-heterogeneity on atmosphere
 1043 and land-surface interactions, *Environ Modell Softw*, 88, 35–47,
 1044 <https://doi.org/10.1016/j.envsoft.2016.11.006>, 2017.
- 1045 Liu, X., Huang, Y., Xu, X., Li, X., Li, X., Ciais, P., Lin, P., et al.: High-spatiotemporal-
 1046 resolution mapping of global urban change from 1985 to 2015, *Nat Sustain*, 3, 564–570,
 1047 <https://doi.org/10.1038/s41893-020-0521-x>, 2020.
- 1048 Lundberg, S. and Lee, S.-I.: A Unified Approach to Interpreting Model Predictions, *Arxiv*, 2017.
- 1049 Lundberg, S. M., Nair, B., Vavilala, M. S., Horibe, M., Eisses, M. J., Adams, T., Liston, D. E.,
 1050 Low, D. K.-W., Newman, S.-F., Kim, J., and Lee, S.-I.: Explainable machine-learning
 1051 predictions for the prevention of hypoxaemia during surgery, *Nat Biomed Eng*, 2, 749–760,
 1052 <https://doi.org/10.1038/s41551-018-0304-0>, 2018.
- 1053 Lundberg, S. M., Erion, G., Chen, H., DeGrave, A., Prutkin, J. M., Nair, B., Katz, R.,
 1054 Himmelfarb, J., Bansal, N., and Lee, S.-I.: From local explanations to global understanding with
 1055 explainable AI for trees, *Nat Mach Intell*, 2, 56–67, <https://doi.org/10.1038/s42256-019-0138-9>,
 1056 2020.
- 1057 Mälicke, M., Hassler, S. K., Blume, T., Weiler, M., and Zehe, E.: Soil moisture: variable in
 1058 space but redundant in time, *Hydrol Earth Syst Sc*, 24, 2633–2653, [https://doi.org/10.5194/hess-](https://doi.org/10.5194/hess-24-2633-2020)
 1059 [24-2633-2020](https://doi.org/10.5194/hess-24-2633-2020), 2020.
- 1060 [Martens, B., Miralles, D. G., Lievens, H., van der Schalie, R., de Jeu, R. A. M., Fernández-](https://doi.org/10.5194/gmd-10-1903-2017)
 1061 [Prieto, D., Beck, H. E., Dorigo, W. A., and Verhoest, N. E. C.: GLEAM v3: satellite-based land](https://doi.org/10.5194/gmd-10-1903-2017)
 1062 [evaporation and root-zone soil moisture, *Geosci. Model Dev.*, 10, 1903–1925,](https://doi.org/10.5194/gmd-10-1903-2017)
 1063 <https://doi.org/10.5194/gmd-10-1903-2017>, 2017.
- 1064 Maxwell, R. M.: A terrain-following grid transform and preconditioner for parallel, large-scale,
 1065 integrated hydrologic modeling, *Adv Water Resour*, 53, 109–117,
 1066 <https://doi.org/10.1016/j.advwatres.2012.10.001>, 2013.
- 1067 Morisette, J. T., Baret, F., Privette, J. L., Myneni, R. B., Nickeson, J. E., et al.: Validation of
 1068 global moderate-resolution LAI products: A framework proposed within the CEOS land product
 1069 validation subgroup, *IEEE Trans Geosci Remote Sens*, 44(7), 1804–1817.
 1070 <https://doi.org/10.1109/TGRS.2006.872529>, 2006.
- 1071 Muñoz-Sabater, J., Dutra, E., Agustí-Panareda, A., Albergel, C., Arduini, G., Balsamo, G.,
 1072 Boussetta, S., Choulga, M., Harrigan, S., Hersbach, H., Martens, B., Miralles, D. G., Piles, M.,
 1073 Rodríguez-Fernández, N. J., Zsoter, E., Buontempo, C., and Thépaut, J.-N.: ERA5-Land: a state-
 1074 of-the-art global reanalysis dataset for land applications, *Earth Syst Sci Data*, 13, 4349–4383,
 1075 <https://doi.org/10.5194/essd-13-4349-2021>, 2021.
- 1076 Myneni, R. B., Hoffman, S., Knyazikhin, Y., Privette, J. L., Glassy, J., Tian, Y., Wang, Y., Song,
 1077 X., Zhang, Y., Smith, G. R., Lotsch, A., Friedl, M., Morisette, J. T., Votava, P., Nemani, R. R.,

1078 and Running, S. W.: Global products of vegetation leaf area and fraction absorbed PAR from
1079 year one of MODIS data, *Remote Sens Environ*, 83, 214–231, [https://doi.org/10.1016/s0034-4257\(02\)00074-3](https://doi.org/10.1016/s0034-4257(02)00074-3), 2002.

1081 Myneni, R., Knyazikhin, Y., Park, T. (2021). MODIS/Terra+Aqua Leaf Area Index/FPAR 4-Day
1082 L4 Global 500m SIN Grid V061 [Data set]. NASA EOSDIS Land Processes DAAC. Accessed
1083 2022-11-21 from <https://doi.org/10.5067/MODIS/MCD15A3H.061>

1084 Naz, B. S., Sharples, W., Ma, Y., Goergen, K., and Kollet, S.: Continental-scale evaluation of a
1085 fully distributed coupled land surface and groundwater model, ParFlow-CLM (v3.6.0), over
1086 Europe, *Geosci Model Dev*, 16, 1617–1639, <https://doi.org/10.5194/gmd-16-1617-2023>, 2023.

1087 Niu, G. Y., Yang, Z. L., Mitchell, K. E., Chen, F., Ek, M. B., Barlage, M., et al.: The community
1088 Noah land surface model with multiparameterization options (Noah-MP): 1. Model description
1089 and evaluation with local-scale measurements, *J Geophys Res Atmos*, 116(D12),
1090 <https://doi.org/10.1029/2010JD015139>, 2011

1091 O’Neill, M. M. F., Tijerina, D. T., Condon, L. E., and Maxwell, R. M.: Assessment of the
1092 ParFlow-CLM CONUS 1.0 integrated hydrologic model: evaluation of hyper-resolution water
1093 balance components across the contiguous United States, *Geosci Model Dev*, 14, 7223–7254,
1094 <https://doi.org/10.5194/gmd-14-7223-2021>, 2021.

1095 Poggio, L., Sousa, L. M. de, Batjes, N. H., Heuvelink, G. B. M., Kempen, B., Ribeiro, E., and
1096 Rossiter, D.: SoilGrids 2.0: producing soil information for the globe with quantified spatial
1097 uncertainty, *Soil*, 7, 217–240, <https://doi.org/10.5194/soil-7-217-2021>, 2021.

1098 Qiu, H., Bisht, G., Li, L., Hao, D., and Xu, D.: Development of Inter-Grid Cell Lateral
1099 Unsaturated and Saturated Flow Model in the E3SM Land Model (v2.0), *Egusphere*, 2023, 1–31,
1100 <https://doi.org/10.5194/egusphere-2023-375>, 2023.

1101 Rabus, B., Eineder, M., Roth, A., & Bamler, R.: The shuttle radar topography mission—A new
1102 class of digital elevation models acquired by spaceborne radar. *ISPRS Journal of*
1103 *Photogrammetry and Remote Sensing*, 57(4), 241–262. [https://doi.org/10.1016/s0924-2716\(02\)00124-7](https://doi.org/10.1016/s0924-2716(02)00124-7), 2003.

1105 Ramankutty, N. and Foley, J. A.: Estimating historical changes in global land cover: Croplands
1106 from 1700 to 1992, *Global Biogeochem Cy*, 13, 997–1027,
1107 <https://doi.org/10.1029/1999gb900046>, 1999.

1108 Rasch, P. J., Xie, S., Ma, P. -L., Lin, W., Wang, H., Tang, Q., Burrows, S. M., Caldwell, P., et
1109 al.: An Overview of the Atmospheric Component of the Energy Exascale Earth System Model, *J*
1110 *Adv Model Earth Sy*, 11, 2377–2411, <https://doi.org/10.1029/2019ms001629>, 2019.

1111 Rastner, P., Bolch, T., Mölg, N., Machguth, H., Le Bris, R., and Paul, F.: The first complete
1112 inventory of the local glaciers and ice caps on Greenland, *The Cryosphere*, 6, 1483–1495,
1113 <https://doi.org/10.5194/tc-6-1483-2012>, 2012.

- 1114 Rizzo, R., Wadoux, A. M. C., Demattê, J. A., Minasny, B., Barrón, V., Ben-Dor, E., ... &
 1115 Salama, E. S. M.: Remote sensing of the Earth's soil color in space and time, *Remote Sens*
 1116 *Environ*, 299, 113845, <https://doi.org/10.1016/j.rse.2023.113845>, 2023.
- 1117 Rouf, T., Maggioni, V., Mei, Y., and Houser, P.: Towards hyper-resolution land-surface
 1118 modeling of surface and root zone soil moisture, *J Hydrol*, 594, 125945,
 1119 <https://doi.org/10.1016/j.jhydrol.2020.125945>, 2021.
- 1120 Ruiz-Vásquez, M., O, S., Arduini, G., Boussetta, S., Brenning, A., et al: Impact of updating
 1121 vegetation information on land surface model performance, *J. Geophys. Res. Atmos.*, 128(21),
 1122 e2023JD039076, <https://doi.org/10.1029/2023JD039076>, 2023.
- 1123 [Running, S., Mu, Q., Zhao, M., Moreno, A. \(2021\). MODIS/Terra Net Evapotranspiration Gap-
 1124 Filled 8-Day L4 Global 500m SIN Grid V061 \[Data set\]. NASA EOSDIS Land Processes
 1125 Distributed Active Archive Center. https://doi.org/10.5067/MODIS/MOD16A2GF.061](https://doi.org/10.5067/MODIS/MOD16A2GF.061)
- 1126 Shangguan, W., Dai, Y., Duan, Q., Liu, B., and Yuan, H.: A Global Soil Dataset for Earth
 1127 System Modeling, *J Adv Model Earth Syst*, 6, 249-263, <https://doi.org/10.1002/2013MS000293>,
 1128 2014.
- 1129 Simard, M., Pinto, N., Fisher, J. B., and Baccini, A.: Mapping forest canopy height globally with
 1130 spaceborne lidar, *J. Geophys. Res. Biogeosci.*, 116, G04021,
 1131 <https://doi.org/10.1029/2011jg001708>, 2011.
- 1132 Singh, R. S., Reager, J. T., Miller, N. L., and Famiglietti, J. S.: Toward hyper-resolution land-
 1133 surface modeling: The effects of fine-scale topography and soil texture on CLM4.0 simulations
 1134 over the Southwestern U.S., *Water Resour Res*, 51, 2648–2667,
 1135 <https://doi.org/10.1002/2014wr015686>, 2015.
- 1136 Slingo, J., Bates, P., Bauer, P., Belcher, S., Palmer, T., Stephens, G., Stevens, B., Stocker, T.,
 1137 and Teutsch, G.: Ambitious partnership needed for reliable climate prediction, *Nat Clim Change*,
 1138 12, 499–503, <https://doi.org/10.1038/s41558-022-01384-8>, 2022.
- 1139 Still, C. J., Berry, J. A., Collatz, G. J., and DeFries, R. S.: Global distribution of C3 and C4
 1140 vegetation: Carbon cycle implications, *Global Biogeochem Cy*, 17, 6-1-6–14,
 1141 <https://doi.org/10.1029/2001gb001807>, 2003.
- 1142 Sulla-Menashe, D., Gray, J. M., Abercrombie, S. P., and Friedl, M. A.: Hierarchical mapping of
 1143 annual global land cover 2001 to present: The MODIS Collection 6 Land Cover product, *Remote*
 1144 *Sens Environ*, 222, 183–194, <https://doi.org/10.1016/j.rse.2018.12.013>, 2019.
- 1145 Swenson, S. C., Clark, M., Fan, Y., Lawrence, D. M., and Perket, J.: Representing Intrahillslope
 1146 Lateral Subsurface Flow in the Community Land Model, *J Adv Model Earth Sy*, 11, 4044–4065,
 1147 <https://doi.org/10.1029/2019ms001833>, 2019.

- 1148 Verdin, K. L. and Greenlee, S. K.: Development of continental scale digital elevation models and
1149 extraction of hydrographic features, paper presented at the Third International Workshop on
1150 Integrating GIS and Environmental Modeling, Santa Fe, New Mexico, 21–26 January, Natl.
1151 Cent. for Geogr. Inf. and Anal., Santa Barbara, Calif, 1996.
- 1152 Vergopolan, N., Chaney, N. W., Beck, H. E., Pan, M., Sheffield, J., Chan, S., and Wood, E. F.:
1153 Combining hyper-resolution land surface modeling with SMAP brightness temperatures to
1154 obtain 30-m soil moisture estimates, *Remote Sens Environ*, 242, 111740,
1155 <https://doi.org/10.1016/j.rse.2020.111740>, 2020.
- 1156 Vergopolan, N., Chaney, N. W., Pan, M., Sheffield, J., Beck, H. E., Ferguson, C. R., Torres-
1157 Rojas, L., Sadri, S., and Wood, E. F.: SMAP-HydroBlocks, a 30-m satellite-based soil moisture
1158 dataset for the conterminous US, *Sci Data*, 8, 264, <https://doi.org/10.1038/s41597-021-01050-2>,
1159 2021.
- 1160 Vergopolan, N., Sheffield, J., Chaney, N. W., Pan, M., Beck, H. E., Ferguson, C. R., Torres-
1161 Rojas, L., Eigenbrod, F., Crow, W., and Wood, E. F.: High-Resolution Soil Moisture Data
1162 Reveal Complex Multi-Scale Spatial Variability Across the United States, *Geophys Res Lett*, 49,
1163 <https://doi.org/10.1029/2022gl098586>, 2022.
- 1164 Wood, E. F., Roundy, J. K., Troy, T. J., Beek, L. P. H. van, Bierkens, M. F. P., et al.:
1165 Hyperresolution global land surface modeling: Meeting a grand challenge for monitoring Earth's
1166 terrestrial water, *Water Resour Res*, 47, <https://doi.org/10.1029/2010wr010090>, 2011.
- 1167 Xia, Y., Mocko, D., Huang, M., Li, B., Rodell, M., Mitchell, K. E., Cai, X., and Ek, M. B.:
1168 Comparison and Assessment of Three Advanced Land Surface Models in Simulating Terrestrial
1169 Water Storage Components over the United States, *J Hydrometeorol*, 18, 625–649,
1170 <https://doi.org/10.1175/jhm-d-16-0112.1>, 2017.
- 1171 Xu, C., Torres-Rojas, L., Vergopolan, N., Chaney, N. W.: The Benefits of Using State-Of-The-
1172 Art Digital Soil Properties Maps to Improve the Modeling of Soil Moisture in Land Surface
1173 Models, *Water Resour Res*, 59(4), e2022WR032336, <https://doi.org/10.1029/2022WR032336>,
1174 2023.
- 1175 Yang, Z. L., Niu, G. Y., Mitchell, K. E., Chen, F., Ek, M. B., Barlage, M., et al.: The community
1176 Noah land surface model with multiparameterization options (Noah-MP): 2. Evaluation over
1177 global river basins, *J Geophys Res Atmos*, 116(D12), <https://doi.org/10.1029/2010JD015140>,
1178 2011.
- 1179 Yamazaki, D., Ikeshima, D., Sosa, J., Bates, P. D., Allen, G. H., and Pavelsky, T. M.: MERIT
1180 Hydro: A High-Resolution Global Hydrography Map Based on Latest Topography Dataset,
1181 *Water Resour Res*, 55, 5053–5073, <https://doi.org/10.1029/2019wr024873>, 2019.
- 1182 Yang, C. and Zhao, S.: A building height dataset across China in 2017 estimated by the spatially-
1183 informed approach, *Sci Data*, 9, 76, <https://doi.org/10.1038/s41597-022-01192-x>, 2022.

- 1184 Yuan, H., Dai, Y., Xiao, Z., Ji, D., and Shangguan, W.: Reprocessing the MODIS Leaf Area
1185 Index products for land surface and climate modelling, *Remote Sens Environ*, 115, 1171–1187,
1186 <https://doi.org/10.1016/j.rse.2011.01.001>, 2011.
- 1187 Yuan, X., Ji, P., Wang, L., Liang, X., Yang, K., Ye, A., Su, Z., and Wen, J.: High-Resolution
1188 Land Surface Modeling of Hydrological Changes Over the Sanjiangyuan Region in the Eastern
1189 Tibetan Plateau: 1. Model Development and Evaluation, *J Adv Model Earth Sy*, 10, 2806–2828,
1190 <https://doi.org/10.1029/2018ms001412>, 2018.
- 1191 Zeng, X., Shaikh, M., Dai, Y., Dickinson, R. E., and Myneni, R.: Coupling of the Common Land
1192 Model to the NCAR Community Climate Model, *J Climate*, 15, 1832–1854,
1193 [https://doi.org/10.1175/1520-0442\(2002\)015<1832:cotclm>2.0.co;2](https://doi.org/10.1175/1520-0442(2002)015<1832:cotclm>2.0.co;2), 2002.
- 1194 Zhao, M., Cheng, C., Zhou, Y., Li, X., Shen, S., and Song, C.: A global dataset of annual urban
1195 extents (1992–2020) from harmonized nighttime lights, *Earth Syst Sci Data*, 14, 517–534,
1196 <https://doi.org/10.5194/essd-14-517-2022>, 2022.
- 1197 Zhou, Y., Li, D., and Li, X.: The Effects of Surface Heterogeneity Scale on the Flux Imbalance
1198 under Free Convection, *J Geophys Res Atmospheres*, 124, 8424–8448,
1199 <https://doi.org/10.1029/2018jd029550>, 2019.